Constraining Variable Accretion in Deeply Embedded Protostars with Interferometric Observations

by

Logan Francis
B.Sc., Saint Mary's University, 2014

A Thesis Submitted in Partial Fulfillment of the
Requirements for the Degree of

MASTER OF SCIENCE

in the Department of Physics and Astronomy

Constraining Variable Accretion in Deeply Embedded Protostars with Interferometric Observations

by

Logan Francis
B.Sc., Saint Mary's University, 2014

Supervisory Committee

Dr. D. Johnstone, Co-Supervisor
(Department of Physics and Astronomy)

Dr. J. Navarro, Co-Supervisor
(Department of Physics and Astronomy)

Supervisory Committee

Dr. D. Johnstone, Co-Supervisor
(Department of Physics and Astronomy)

Dr. J. Navarro, Co-Supervisor
(Department of Physics and Astronomy)

ABSTRACT

Variability of pre-main-sequence stars observed at optical wavelengths has been attributed to fluctuations in the mass accretion rate from the circumstellar disk onto the forming star. Detailed models of accretion disks suggest that young deeply embedded protostars should also exhibit variations in their accretion rates, and that these changes can be tracked indirectly by monitoring the response of the dust envelope at mid-IR to millimeter wavelengths. Interferometers such as ALMA offer the resolution and sensitivity to observe small fluctuations in brightness at the scale of the disk where episodic accretion may be driven. In this thesis, novel methods for comparing interferometric observations are presented and applied to CARMA and ALMA 1.3mm observations of deeply embedded protostars in Serpens taken 9 years apart. No brightness variation is found above the limits of the analysis of a factor of $\gtrsim 50\%$, due to the limited sensitivity of the CARMA observations and small number of sources common to both epochs. It is further shown that follow up ALMA observations with a similar sample size and sensitivity may be able to uncover variability at the level of a few percent, and the implications of this for future work are discussed.

Contents

List of Tables

List of Figures

Acknowledgements

I would like to thank:

Doug Johnstone, Steve Mairs, Helen Kirk, and Michael Dunham for their mentoring and support throughout the past two years.

Todd Hunter, Sümeyye Suri, Laura Perez, John Carpenter, and Gerald Scheiven for their useful insights on this project and support with ALMA and CARMA data reduction.

The folks on Arbutus road for making Victoria a wonderful home.

Coffee, beer, music, and the great outdoors for moral support.

Chapter 1

Introduction and Background

1.1 Thesis Overview

This thesis is organized as follows: In chapter 1, star formation in our Galaxy is reviewed and the problem of understanding variable accretion processes in young stellar objects from an observational perspective is presented. A brief review of the imaging process for radio interferometers is also given to provide context for the methods used in this work. In chapter 2, data reduction for the ALMA and archived CARMA observations of Serpens Main used is detailed, and high-resolution maps of the deeply embedded protostars produced from the ALMA data are described. In chapter 3, the ALMA observations are compared against themselves to determine sensitivity limits of future ALMA campaigns for detecting variability under ideal conditions. In chapter 4, novel techniques for comparing interferometric observations are presented and applied to the ALMA and CARMA data in order to search for variability between the two epochs. In chapter 5, the results and detection limits of this variability study are discussed, and ideal directions for future variability studies are highlighted. In the Appendix, the brightness and structure of the deeply embedded protostars detected by ALMA are discussed in the context of past and recent observations. Chapters 2-5 of this thesis form the basis of a paper ("Identifying Variability in Deeply Embedded Protostars with ALMA and CARMA") submitted to the Astrophysical Journal on Sept 10^{th} 2018.

1.2 Star Forming Environments and Processes

Under dark skies, the plane of our Galaxy is easily seen arching across the sky. Two features of the Galaxy are immediately apparent: the greatly increased concentration

Table 1.1. Properties of Clouds, Clumps, and Cores

	Clouds	Clumps	Cores
Mass ($M_\odot$)	$10^3 - 10^4$	$50 - 500$	$0.5 - 5$
Size (pc)	$2 - 15$	$0.3 - 3$	$0.03 - 0.2$
Mean Density (cm^{-3})	$50 - 500$	$10^3 - 10^4$	$10^4 - 10^5$
Gas Temperature (K)	≈ 10	$10 - 20$	$8 - 12$

Note. — Adapted from table 1 of (Bergin & Tafalla, 2007).

of stars, and the presence of dark clouds obscuring the light from stars behind them. These two casual observations are not unconnected — the dark clouds we see are in fact giant clouds of cold molecular Hydrogen and dust, which provide both the raw materials and environment for star formation to occur. Deeper observations with optical telescopes find young stars associated with the molecular clouds from which they have presumably been recently born. At near-infrared and longer wavelengths, the obscuring dust becomes more transparent, and protostars still forming from the clouds gas can be seen within the molecular cloud. While the general picture of how molecular cloud gas is turned into these stars is now understood, a great number of details remain uncertain. Here, a broad review of the properties of molecular clouds will be provided, followed by a discussion of the formation of protostars by gravitational collapse and their subsequent evolution into main-sequence objects.

1.2.1 Molecular Cloud Properties

Molecular clouds are mostly found within the spiral arms of the Galaxy, with average densities and temperatures ranging from 100 to 500 cm^{-3} and 10 to 40 K (Heyer & Dame, 2015). At these temperatures, the H_2 gas which comprises the bulk of the cloud can not be easily detected in any of its rotational transitions. Instead, indirect means must be used to trace the presence of H_2. One particularly successful method is to instead observe rotational transitions excited in other molecules present in the cloud, such as the sub-mm and mm transitions of CO. Molecular tracers also provide valuable dynamical information through the Doppler shifting and broadening of their spectral lines. Another method is to map the dust component of the cloud, which can

also be used to estimate the H_2 content provided an appropriate dust-to-gas ratio. In optical and near-IR regimes, the dust mass can be estimated from extinction of background starlight, while in the densest and highly extincted regions of the cloud, thermal continuum emission from optically thin dust at sub-mm/mm wavelengths becomes a more suitable tracer.

Using these tracers of H_2, much has been learned about the structure and properties of molecular clouds. They typically have an irregular appearance and contain long filamentary structures, which often converge at sites of active star formation (Bergin & Tafalla, 2007). In their large scale velocity structure, molecular clouds are found to exhibit supersonic motions with no apparent pattern, suggesting turbulent motion. The presence of turbulence is further evidenced by empirical scaling relationships which show larger clouds to have higher overall velocity dispersions, as expected from analytical models of the turbulence power spectrum (Larson, 1981). Polarization and Zeeman splitting measurements show molecular clouds to be threaded by magnetic fields, which may have important implications for determining the cloud structure and providing additional support against gravitational collapse, however, the importance of the magnetic field contribution is unclear due to observational difficulties in obtaining reliable measurements of the field properties. Molecular clouds exhibit a hierarchical structure, with smaller and denser sub-units embedded within larger ones. Molecular clouds are typically described as containing "clumps", which in turn contain "(dense) cores" (Williams et al., 2000), although the hierarchical structure can also be quantified using fractal geometry (Bergin & Tafalla, 2007). The basic properties of clouds, clumps and cores are summarized in table 1.1. The masses of clumps and cores are such that the collapse of a core would result in a (low to intermediate mass) star (or multiple star system), while the collapse of the many cores within a clump would produce a star cluster. Cores are thus the basic units of star formation, the properties of which determine the initial conditions for star formation. Some cores are found to already contain deeply embedded YSOs within them, further demonstrating their role in star formation.

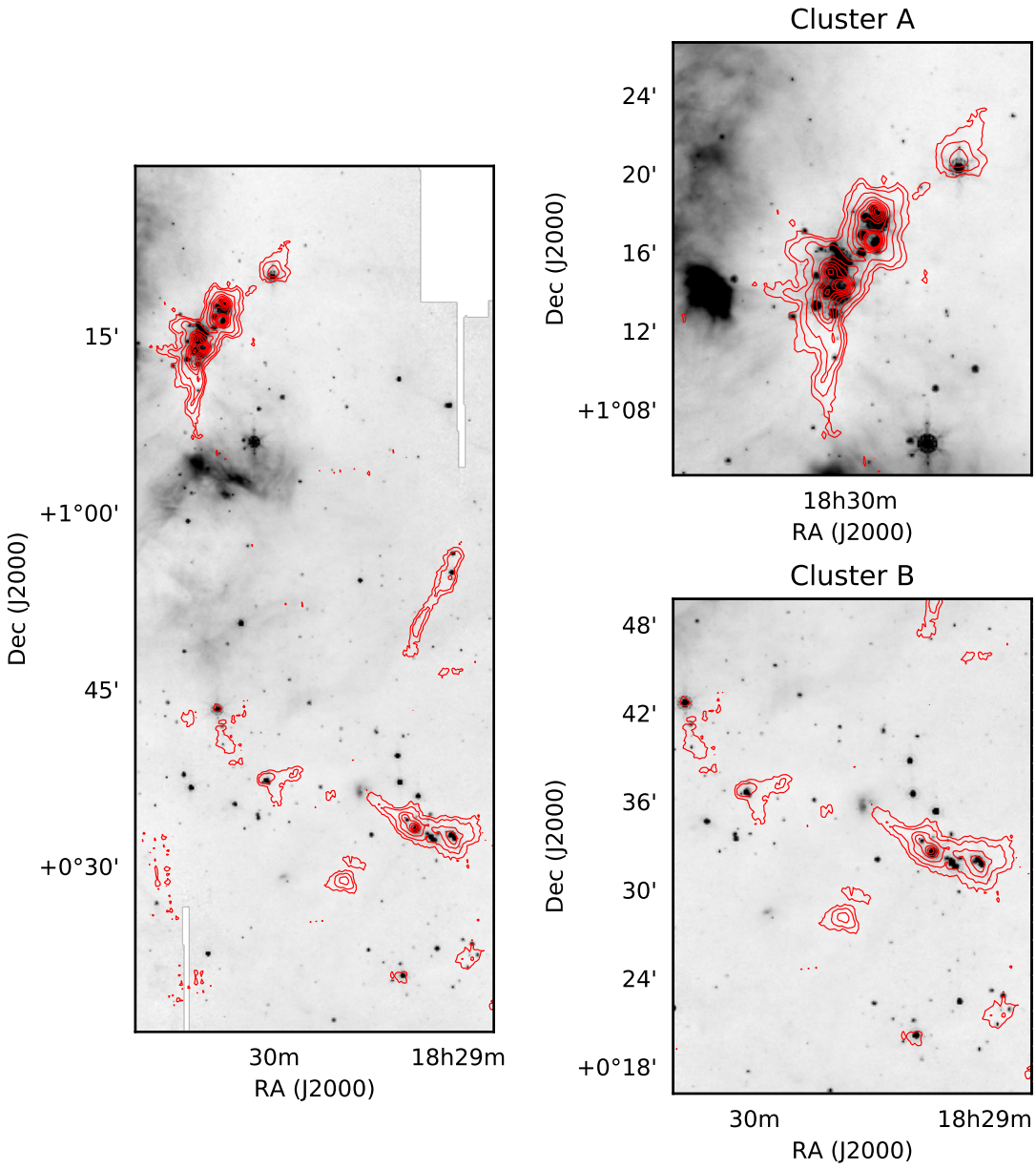

Figure 1.1 The Serpens Main molecular cloud observed at mid-IR and mm wavelengths. Inverted greyscale displays emission in the Serpens Main molecular cloud from 24 μm Spitzer continuum maps (Harvey et al., 2007) while overlaid red contours show 1.3 mm emission from Caltech Submillimetre Observatory (CSO) Bolocam maps (Enoch et al., 2007). The blown up panels on the right show the two densest clusters of embedded star formation.

One particular example of an active star forming region (and the area containing

the objects studied in this work) is the Serpens Main molecular cloud[1]. The Serpens Main cloud is located 436.0 ± 9.2 pc away (Ortiz-León et al., 2017) and spans several degrees near the variable star VV Ser, and is part of the much larger Aquila rift dark cloud complex (Eiroa et al., 2008). Figure 1.1 shows Spitzer 24 μm observations of Serpens Main (greyscale) overlaid with Bolocam 1.1 mm data (red contours). The mm emission is mostly produced by cold ($\sim$ 10 K) dust and traces the denser clumps and cores, while the 24 μm emission originates from warm (100-1000 K) dust and embedded YSOs. The combined maps show several distinct clumps containing embedded YSOs; the Northern embedded cluster is known as the Serpens Main Core (or Cluster A), while the Southern is called the Serpens G3/G6 (or Cluster B) region.

1.2.2 Theoretical Cloud Collapse and YSO evolution

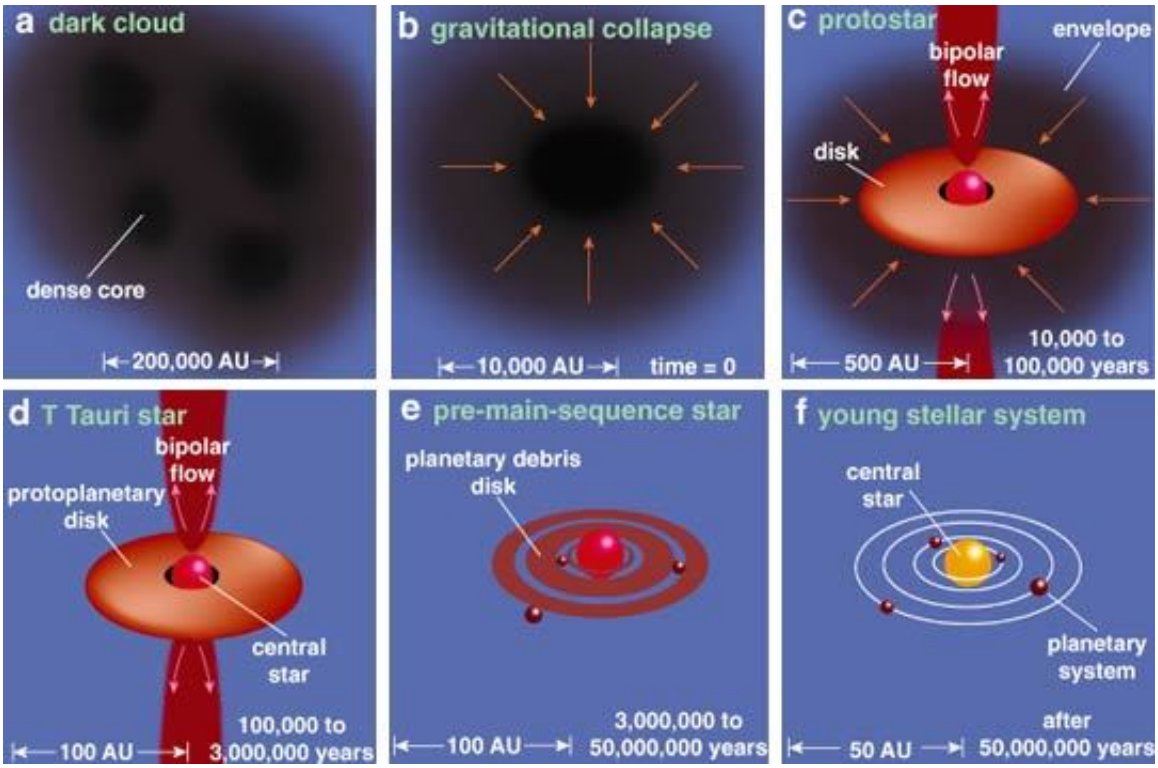

Figure 1.2 Schematic description of the process by which a dense core collapses to form a low to intermediate mass star (Greene, 2001).

[1]Also referred to as simply the Serpens Molecular cloud in older literature. The "Main" prefix distinguishes this region from the Serpens South cluster of embedded stars located $\sim$ 3 degrees to the South, which was discovered more recently through observations by the Spitzer Space Telescope.

The process by which a dense core becomes a low to intermediate mass star system is shown schematically in figure 1.2. In panel a, a molecular cloud clump containing dense cores is shown. The stability of a dense core (or more generally, a larger clump or cloud) depends on the competition between gravity and the supporting effects of the cloud's motion, thermal pressure, and magnetic fields. This can be described physically by the energy supplied by these competing forces using the virial theorem for an equilibrium state:

$$0 = 2\mathcal{T} + 2\mathcal{U} + \mathcal{W} + \mathcal{M}, \tag{1.1}$$

where $\mathcal{T}$, $\mathcal{U}$, $\mathcal{W}$, and $\mathcal{M}$ are respectively the kinetic energy in bulk motion (e.g., from rotation of the cloud), thermal energy, gravitational potential energy, and the energy associated with the cloud's magnetic fields. The gravitational potential energy $\mathcal{W}$ is negative while the other energies in equation 1.1 are always positive, indicating their opposite effects on the cloud's equilibrium state. If the combination of $\mathcal{T}$, $\mathcal{U}$, and $\mathcal{M}$ does not exceed $\mathcal{W}$, the cloud will be unstable to collapse.

Useful conditions for the maximum mass and extent (The *Jean's* mass and length) of a cloud or core can be derived by applying the virial theorem[2] to models of clouds and cores. A simple yet still informative model is an un-magnetized sphere of gas in hydrostatic equilibrium, with an isothermal equation of state. For this model, the Jean's mass M_J and length R_J are

$$M_J = \left(\frac{5kT}{Gm}\right)^{3/2} \left(\frac{3}{4\pi\rho}\right)^{1/2}, R_J = c_s\sqrt{\frac{9}{4\pi}\frac{1}{G\rho}}. \tag{1.2}$$

where k and G are the Boltzmann and gravitational constants, m, ρ, and T are the cloud's mean mass per particle, density and temperature, and c_s is the sound speed. Cores more massive than the Jean's mass (or larger than the Jean's length) are unstable, and will collapse under their own gravity.

There are several caveats to applying equations 1.2 to observations. An isothermal equation of state is only appropriate for clouds which are optically thin to most of their own radiation, which is not the case for denser structures. The effects of rotation and magnetic fields have also been ignored, although analogous Jean's quantities can be derived which take these into account. A cloud in uniform rotation can provide support against collapse, but only perpendicular to its rotation axis. Observations

[2] Alternatively, one can compare the free fall time (the time for the cloud to collapse with in the absence of any resisting pressure) to the sound crossing time on which thermal pressure reestablishes equilibrium. If the sound crossing time is shorter than the free fall time, the cloud will collapse.

show dense cores are generally not rotating fast enough for rotation to be a significant source of support, but rotation does result in the formation of an accretion disk around the YSO during the collapse. Magnetic fields are also a potential source of support for the cloud. Field lines threading a cloud act on its ionized component, and will resist being squeezed together. However, neutral particles are not affected by magnetic fields, and the field lines can gradually slip out of the cloud by the process of ambipolar diffusion, rendering the cloud unstable. Finally, clouds and cores do not exist in isolation, and compressive perturbations, e.g., from a passing spiral density wave in a galaxy or from a supernova shock, can also induce collapse.

Once a core becomes unstable, the collapse process in panel b of figure 1.2 proceeds in a self-similar and inside-out manner (Shu, 1977; Shu et al., 1987). A protostar forms at the center of the core as mass begins to fall in from increasingly far out in the envelope. Rotation of the core and conservation of angular momentum causes material from farther out in the envelope to eventually miss the star and form an accretion disk instead. Further growth of the protostar (panel c) proceeds largely by accretion from the disk (see section 1.3). During the protostar phase, accretion onto the stellar surface should produce most of the luminosity. If the all of the gravitational energy in the infalling mass goes into heating the disk and envelope, the luminosity of the protostar due to accretion $L_{\rm acc}$ should be

$$L_{\rm acc} = GM_*\dot{M}_*/R_*, \tag{1.3}$$

where M_*, $\dot{M}$, and R_* are respectively the mass, accretion rate, and radius of the protostar. But, in what has become known as the "luminosity problem"(Kenyon et al., 1990; Dunham et al., 2010, 2014), the observed luminosities of protostars are found to be spread over several orders of magnitude (Dunham et al., 2015; Jensen & Haugbølle, 2018) and extend to much lower levels than expected from equation 1.3. Possible solutions to this luminosity problem are discussed in section 1.3.

The protostar phase ends when most of the mass in the envelope has been accreted by the protostar or dispersed in winds and outflows (panel d). This marks the beginning of the pre-main-sequence (PMS) phase of evolution. During this phase, the luminosity of the PMS star is produced mostly as a result of gravitational contraction. While the central temperatures in low mass PMS stars are not yet hot enough to burn Hydrogen, Deuterium fusion does occur, however, the overall luminosity from deuterium burning is low. In younger PMS stars (e.g., T-Tauri stars, see below),

an accretion disk remains from the protostellar phase, which gradually becomes dispersed. The PMS phase ends with the onset of central Hydrogen burning in the star and evolution onto the main sequence.

From an observational perspective, The YSOs in Serpens Main span a variety of stages in their evolution discussed above. A general feature of YSOs indicative of their youth is the presence of excess infrared emission (i.e., above that expected from the stellar photosphere) in their spectra. The IR excess is caused by emission from circumstellar dust warmed by the YSO, and signifies the presence of material remaining from the collapse process in an accretion disk or envelope surrounding the YSO. More evolved YSOs should have accreted more of their mass, and therefore should also have less of an IR excess. Observational classifications of YSOs thus measure the amount of IR-excess as a relative indicator of the YSO age. This is done using the (extinction corrected) IR spectral index $\alpha = \frac{d\log(\lambda S_\lambda)}{d\log(\lambda)}$ (Greene et al., 1994) or the bolometric temperature (T_{bol}), the temperature of a black-body with the same mean frequency as the observed spectrum[3] (Myers & Ladd, 1993; Chen et al., 1995). Using the bolometric temperature, the observed classes are defined as:

- Class 0: $T_{\rm bol} \leq 70$ K and significant sub-mm emission;
- Class I: 70 K $< T_{\rm bol} \leq 650$ K;
- Class II: 650 K$< T_{\rm bol} \leq 2800$ K;
- Class III: $T_{\rm bol} > 2800$ K.

Class 0 YSOs are an addition to the original classification scheme based on the discovery of objects so deeply embedded that they can not be seen at less than 10 μm. In addition to being the coldest and least evolved YSOs, Class 0 objects are also often seen driving energetic outflows, which is likely evidence of their high accretion rates. In general, objects with earlier YSO Classes are more likely to be in the protostellar phase of their evolution, where accretion still provides most of the object's luminosity. Later types are more likely in the pre-main-sequence (PMS) phase of their evolution, after most of the envelope mass has been accreted, but before Hydrogen fusion has begun. T-Tauri and Herbig Ae/Be stars are types of PMS stars which typically fall into Class II or III. T-Tauri stars are low (0.08-2M$_\odot$) mass, optically visible PMS

[3]The bolometric temperature is used instead of an effective temperature as the surroundings of a YSO contain dust and gas emitting at a wide range of temperatures, unlike the single temperature which characterizes a stellar photosphere.

stars with an IR excess and Hα emission lines from a circumstellar disk, while Herbig Ae/Be stars are essentially intermediate mass (2-10$M_\odot$) analogs to T Tauri stars.

1.3 Variable Accretion in Young Stellar Objects

Although the picture of how stars form given in section 1.2 is broadly correct, the details of how a YSO gathers mass during the protostellar phase (panel c of figure 1.2) are still relatively poorly understood. In order for the protostar to grow by accretion from the disk, material in the disk must lose sufficient angular momentum to reach the stellar surface. In any stable circumstellar disk, the angular velocity must decrease radially outward. If there is some source of internal viscosity in the disk, torques between neighbouring annuli will simultaneously spin up the material in the exterior annulus while spinning down that in the interior. This transports angular momentum outward, and thus allowing mass in the interior annulus to accrete onto the stellar surface.

Two mechanisms which are likely to provide a source of viscosity in the disk are the gravitational and magneto-rotational instabilities (MRI). In the gravitational instability, a radially extended mass concentration becomes sheared out into a trailing spiral arm, and gravitational forces between the inner and outer regions of the arm can provide an effective viscosity to transport angular momentum outward. For gravitational instability to occur, the disk must be a significant fraction of the stellar mass, and thus this is more likely to occur during the earlier part of the protostellar phase. In the magneto-rotational instability, viscosity is provided by stretching of magnetic field lines threading a partially ionized disk in the radial direction. Faster rotating material in the inner disk will drag the field lines with it, and the magnetic field will try to resist the shearing, providing the torques needed to transport angular momentum. The MRI is not effective within interior regions of the disk which are shielded from ionizing radiation from the protostar, however. Whether gravitational or magneto-rotational instability plays a larger role in angular momentum transport remains unclear due to the difficulties in observing embedded disks (see review by Hartmann et al. (2016)).

A key aspect of protostellar accretion which is also poorly constrained by observations is variation in the accretion rate $\dot{M}$. A wide variety of mechanisms in numerical models predict an unsteady accretion rate, including the gravitational and/or magneto-rotational instabilities discussed above (e.g., Armitage et al. 2001; Vorobyov

& Basu 2005, 2006, 2010; Machida et al. 2011; Cha & Nayakshin 2011; Zhu et al. 2009a,b, 2010; Bae et al. 2014), quasi-periodic magnetically driven outflows in the envelope (Tassis & Mouschovias, 2005), decay and regrowth of magneto-rotational instability turbulence (Simon et al., 2011), close interaction in binary systems or in dense stellar clusters (Bonnell & Bastien 1992; Pfalzner et al. 2008), and disk/planet interactions (Lodato & Clarke 2004; Nayakshin & Lodato 2012).

A variable accretion rate can also resolve the luminosity problem described in section 1.2. If a large portion of a protostar's mass is accreted in episodes occupying a small fraction (< 0.01) of its lifetime, the luminosity problem vanishes. However, this is not the only plausible solution; a longer protostellar lifetime with a lower or exponentially decreasing accretion rate caused by the finite size of the envelope or effects of outflows may also resolve or alleviate the luminosity problem (McKee & Offner, 2011).

Despite the abundance of possible theoretical origins for variable accretion rates in young stars, and the likelihood that accretion occurs at a wide range of amplitudes and frequencies (e.g. Vorobyov & Basu 2010), most observational constraints come from indirect evidence or rarely observed large amplitude bursts followed over the course of years. The strongest indirect evidence of variability is found in the clumpy structure of outflows driven by young protostars (e.g. Plunkett et al. (2015)) and their signatures in the envelope chemistry [(Taquet et al., 2016; Rab et al., 2017), see also reviews in Dunham et al. (2014)]. Two examples of types of bursts at optical wavelengths are FUors and EXors, classes of young T-Tauri stars which are observed to brighten by several magnitudes and remain bright for decades (FUors) or months to years (EXors) (Herbig, 1977; Hartmann & Kenyon, 1996; Herbig, 2008). This rise in brightness of FUors is interpreted as an increase in the accretion rate from the disk by factors of $10^2 - 10^4$ (Reipurth, 1990), and is believed to occur only a few times during the formation of a star (Audard et al., 2014). More evolved T-Tauri stars are also inferred to exhibit regular changes in their accretion rate by factors of a few from variations in emission line strength (Costigan et al., 2014; Venuti et al., 2015).

While changes in the brightness of older T Tauri stars can be monitored in the optical or near-IR, protostars in the earliest stages of their evolution are too deeply embedded in their nascent envelopes to be directly observed. At far-IR to mm wavelengths, the bulk of the dust in the disk and envelope (heated by the protostar) is optically thin to its own emission, and the bolometric luminosity of the system can be obtained. Johnstone et al. (2013) used models of deeply embedded protostars under-

going sharp increases in their accretion luminosity to show that the envelope heats up in response to a burst on a timescale of days to months, with the largest and fastest changes in luminosity occurring at the effective photosphere of the envelope around $\sim$ 100 AU. In the far-IR near the peak of the SED ($\sim$ 100 μm), the observed flux can be used as a direct measure of the accretion rate as a proxy for the bolometric luminosity. At sub-mm/mm wavelengths, changes in the flux probe variability in the disk and envelope temperature, resulting in a somewhat weaker response.

Until recently, only a handful of large amplitude bursts onto deeply embedded protostars have been detected in the far-IR to mm, and these detections have all been serendipitous. The protostar HOPS 383 was the first Class 0 protostar found to have undergone an accretion burst, brightening by a factor of $\sim$ 35 at 24μm (Safron et al., 2015) and a factor of $\sim$ 2 in the sub-mm. An outburst at mm wavelengths of a factor of $\sim$ 4 was found in the massive ($\sim 50-156$ M$_\odot$) and distant (1.3 ± 0.09 kpc) protostellar system NGC 6334-I by comparing 2008 Submillimeter Array (SMA) and 2015 Atacama Large Millimeter/submillimeter Array (ALMA) observations, corresponding to an increase in luminosity by a factor of $\sim$ 70 (Hunter et al., 2006, 2017). Liu et al. (2017) conducted a 1.3 mm SMA survey of FUors and similar outbursting objects, and very tentatively detected 30-60% variability over a period of $\sim$1 year in V2494 Cyg and V2495 Cyg.

The ongoing James Clerk Maxwell Telescope (JCMT) Transient Survey (Herczeg et al., 2017) is the first survey designed to monitor for variability in young stellar objects (YSOs) at sub-mm wavelengths. Eight nearby ($<$ 500 pc) star forming regions are being monitored at a monthly or better cadence with the Submillimetre Common-User Bolometer Array 2 (SCUBA-2; Holland et al. 2013) at 450 and 850 μm. As the absolute flux calibration of SCUBA-2 is at the very best $\sim$ 10% (450 μm) or $\sim$ 5% (850 μm) (Dempsey et al., 2013), a relative flux calibration strategy requiring identification and use of stable calibrators in the field is used, and currently achieves a relative calibration accuracy of $\sim$ 2% at 850 μm across epochs (Mairs et al., 2017a).

The first half of the 36 month Transient Survey has found that in a sample of 51 protostars brighter than 350 mJy/beam at 850 μm (14.6$''$beam), 10% are varying at rates of $\sim |5|\%\mathrm{yr}^{-1}$. Several of the most robust variables are found in the Serpens Main molecular clouds, including EC53, SMM10, and SMM1. EC 53 is a Class I protostar already known to be a variable at 2μm (Hodapp, 1999; Hodapp et al., 2012) and which varies at 850 μm by $\sim$50% with an $\sim$18 month period, interpreted as accretion flow mediated by a companion star or planet at several AU (Yoo et al.,

2017). The Class 0/I object SMM10 is found to have a fractional increase in peak brightness of$\sim 7\%\mathrm{yr}^{-1}$ (Johnstone et al., 2018). SMM1, a bright intermediate mass Class 0 protostar, is rising in brightness by $\sim 5\%\mathrm{yr}^{-1}$, (Johnstone et al., 2018; Mairs et al., 2017b), and 0.3″ALMA observations show it to harbour a high velocity CO jet (Hull et al., 2016). HOPS 383, the serendipitous source in Orion detected by Safron et al. (2015), now appears in decline (Johnstone et al., 2018; Mairs et al., 2017b).

While the Transient Survey monitors a large number of sources over several years, the beam size of the JCMT at the distances of several hundred pc in the surveyed fields (Herczeg et al., 2017) includes much of the outer envelope in the beam, rather than just the effective photosphere surrounding the disk near ~ 100 AU where changes in the accretion luminosity are most prominent (Johnstone et al., 2013). This results in dilution of the signal and possible contamination by heating from the interstellar radiation field. Given that the Transient Survey is still able to find variations at the level of $\sim |5|\%\mathrm{yr}^{-1}$, higher resolution observations examining the disk and inner envelope with similar calibration uncertainty should be more sensitive to variability. Interferometric observations can provide both the high resolution and sensitivity needed, as well as spatial filtering out of large scale emission from the outer envelope.

1.4 Interferometric Observing in Radio Astronomy

Observing with an interferometer introduces additional inherent complications not seen with single dish telescopes. In order to compare interferometric observations and search for variability, the basics of aperture synthesis and image reconstruction must be well understood. Here, a brief review of these subjects is provided as context for the new methods discussed in chapter 4.

The use of interferometry in radio astronomy is motivated by the difficulty of achieving high resolution at typical radio wavelengths. The Rayleigh criterion for achieving an angular resolution is $\theta = 1.22\frac{\lambda}{D}$, where λ and D are respectively the wavelength and aperture diameter. At a near-IR wavelength of 1000 nm, obtaining a (diffraction limited) 1″ resolution requires a ~ 0.25 m aperture. At wavelengths of 1 mm and 1 cm (typical of ALMA and the Very Large Array (VLA) respectively), the same resolution would require expensive and impractical apertures of ~ 250 m and ~ 2500 m. An interferometer overcomes this problem by instead combining astronomical signals from many individual smaller antennas in an array to reach an effective resolution of $\theta \sim \lambda/B_{\mathrm{max}}$, where B_{max} is the maximum baseline separation

between any pair of antennas. Thus, arbitrary levels of resolution can be achieved by simply placing antennas in the array further apart, subject to some practical and calibration limitations.

Interferometric observations are more complicated than those with single dish telescopes because they do not directly produce an image of the source under observation. Instead, an interferometer measures the Fourier Transform of the sky intensity distribution, the complex *visibility*. The visibility function is defined as

$$V(u,v) = \mathcal{F}\{A(x,y)I(x,y)\} \tag{1.4}$$

where $A(x,y)$ and $I(x,y)$ are the sensitivity of the antenna and intensity as functions of the offset East (x) and North (y) from the observing center, and where $V(u,v)$ is the complex visibility as a function of the spatial frequencies in the East (u) and North (v) directions. To measure the visibility function, each pair of antennas (baseline) in the array amplifies and digitally samples signals from the observed source during an integration (typically of order 1s), which are then multiplied together in a supercomputer (the correlator) to produce samples of V called visibilities. The amplitude of each complex visibility indicates the amount of power in the mode with spatial frequency u and v, while their phase is related to the direction radiation is incident along a baseline.

The location of a given visibility in the uv-plane is the baseline length in units of the observing wavelength λ as seen from the perspective of the observed source. Points in the uv plane are related to angular scales on the sky by the inverse of their distance from the origin. Thus, short baselines sample visibilities near the center of the uv-plane corresponding to large scale emission on the sky, while long baselines sample visibilities at large uv-distances and measure fine detail. During the course of typical observation, the earth rotates and the orientation and degree of foreshortening of each baseline relative to the source changes. As a result, each baseline will produce visibilities in an elliptical track through the uv-plane, resulting in better sampling.

To obtain an image of a source, all of the collected visibilities can simply be Fourier transformed. Radio astronomers describe this as a "dirty" image, as the incomplete sampling of the uv-plane produces artefacts in the resulting image. In mathematical terms, the dirty image I_D is the convolution of the true sky intensity distribution I

with the Fourier transform of the (weighted) uv-plane sampling function $S(u, v)$:

$$\mathcal{F}\{WSV\} = \mathcal{F}\{WS\} \circledast \mathcal{F}\{V\} = B \circledast I = I_D. \tag{1.5}$$

Here, $W(u, v)$ is an optional weighting applied to each visibility, and $B = \mathcal{F}\{WS\}$ is the synthesized (or dirty) beam. The synthesized beam of an observation is exactly analogous to the point spread function (PSF) of a filled aperture telescope. The typical PSF for a filled aperture however, is approximately an Airy disk, which results from the complete sampling of all spatial scales up to the smallest allowed by the aperture diameter. Since the sampling of spatial frequencies in an interferometer is always incomplete, it can be seen that the cost of obtaining higher resolution is a synthesized beam shape which is usually significantly poorer than an Airy disk.

The synthesized beam shape can be improved to some extent by observing for a longer period to better fill in the uv-plane, and by combining visibilities from array configurations with different antenna spacings. There will nevertheless be gaps in the uv-coverage remaining, particularly in the center of the uv-plane, which can not be sampled because of physical limits on how close two antennas can be placed together. The remaining effects of poor sampling can be mitigated by using deconvolution algorithms to produce an image of the source. As the name suggests, deconvolution algorithms attempt to remove the undesirable artefacts caused by convolution of the dirty beam with the true sky intensity. The classic algorithm for deconvolution in radio astronomy is CLEAN (Högbom, 1974), descendents of which are still widely used. The procedure for CLEAN is as follows:

1. Form a dirty image from the visibilities and initialize an empty model image of the sky.

2. From the brightest point in the dirty image, subtract the dirty beam scaled by a small factor γ (usually between 0.1-0.5) to create a residual image. Simultaneously, add a Dirac delta function of amplitude γ to the model image.

3. Repeat step 2, but using the residual image from the previous iteration in place of the dirty image. Stop when the brightest point in the residual image is below some threshold value, typically a factor of a few times the noise level in the map.

4. Convolve the model image with an idealized "clean" beam (typically a Gaussian

fit to the primary lobe of the dirty beam) and add the residual image to the model.

The resulting "cleaned" image has significantly improved sensitivity and fewer artefacts than the original dirty image, allowing much fainter sources to be detected. CLEAN effectively interpolates between the measured visibilities, and has been shown to converge to a least-squares fit of sinusoids to the visibilities in the absence of noise Schwarz (1978). Many variants in the basic procedure have been developed, with improvements in efficiency (Clark, 1980), handling of frequency-dependent changes in beam shape (Conway et al., 1990), cleaning of extended emission (Cornwell, 2008), and more. However, all of these approaches still essentially follow the iterative procedure described above.

Aside from the uv-plane sampling $S(u, v)$, the synthesized beam shape only depends upon the weighting of each visibility $W(u, v)$. Individual visibilities are typically assigned an estimate value of their RMS noise σ based on their integration time and the frequency channel width. The value of σ is further increased during calibration if the visibilities are found to be noisier than expected. Each visibility is then assigned a weight of σ^{-2} to maximize the use of the most sensitive data. When images are produced from the visibilities, these weights can be used in a variety of ways. In the natural scheme, the weights are simply used as is, resulting in an image with maximum point source sensitivity. With a uniform weighting scheme, the weights are rescaled so that poorly sampled regions of the uv-plane receive more weight. This improves the shape of the synthesized beam and the resolution of the image, but increases the noise level in the image. The Briggs scheme (Briggs, 1995) attempts to find a good compromise between natural and uniform weighting and allows a continuous variation between either scheme through its robust parameter. The robust parameter can be set anywhere between -2 and 2, which at the extremes are effectively identical to uniform and natural weighting respectively.

Chapter 2

ALMA and CARMA Observations

The ALMA observations used in this work are designed to measure the 1.3 mm flux of a sample of deeply embedded protostars for which a previous epoch exists in order to identify any large amplitude ($> 50\%$) variations, and as a baseline for comparisons with future ALMA observations which may uncover much lower levels of variability. The targets are 12 Class 0 and I sources in the Serpens Main molecular cloud (table 2.1) previously identified in comparisons of Bolocam and Spitzer maps (Enoch et al., 2009) and mapped at high angular resolution ($\sim 1''$) with CARMA from 2007-2010 (Enoch et al., 2011). One of these sources (SMM1/Ser-emb 6) is a known Class 0 variable protostar identified by the Transient Survey.

The Serpens Main star forming region is located 436.0 ± 9.2 pc away (Ortiz-León et al., 2017) and contains 34 Class 0 and I protostars (Dunham et al., 2015). The high resolution CARMA maps of Serpens Main covered the 9 known Class 0 and 3 marginal Class I sources (Enoch et al., 2009) in order to constrain the disk and envelope structure of the youngest protostars. Of the 12 sources observed with CARMA, only 9 were robustly detected in preliminary 110 GHz (2.7 mm) and followed up with 230 GHz (1.3 mm) observations.

2.1 ALMA Observations and Calibration

233 GHz (1.3 mm) Band 6 continuum observations of the Serpens sources in table 2.1 were taken in July 2016 using the ALMA C36-6 configuration to provide $0.3''$resolution; further details of the observing setup are listed in table 2.2. Flux and bandpass calibrators were observed at the beginning of the schedule, followed by science observations for each target interlaced with (phase) gain calibrators. Each science target was observed in two separate scans of equal length (except Ser-emb 5,

Table 2.1. Embedded Protostars observed by ALMA and CARMA

Source Name	ALMA Pointing Center	Class[a]	CARMA 230 GHz Map?	Other Names
Ser-emb 1	18:29:09.09 +00.31.30.9	0	Y	
Ser-emb 2	18:29:52.44 +00.36.11.7	0	N	
Ser-emb 3	18:28:54.84 +00.29.52.5	0	N	
Ser-emb 4[b](N)	18:30:00.30 +01.12.59.4	0	Y	
Ser-emb 5	18:28:54.90 +00.18.32.4	0	Y	
Ser-emb 6	18:29:49.79 +01.15.20.4	0	Y	SMM1, FIRS1
Ser-emb 7	18:28:54.04 +00.29.29.7	0	Y	
Ser-emb 8	18:29:48.07 +01.16.43.7	0	Y	S68N
Ser-emb 9	18:28:55.92 +00.29.44.7	0	N	
Ser-emb 11[b](W)	18:29:06.61 +00.30.34.0	I	Y	
Ser-emb 15	18:29:54.30 +00.36.00.8	I	Y	
Ser-emb 17	18:29:06.20 +00.30.43.1	I	Y	

[a]Division between Class 0 and I determined by Enoch et al. (2009). The analysis of (Dunham et al., 2015) places all of these protostars in a combined Class "0+I" category.

[b]Source has multiple components in CARMA observations.

Table 2.2. ALMA Observing Setup

Parameter	Value
Observation date(s)	21 July 2016
Configuration	C36-6
Number of Antennas	39
Project code	2015.1.00310.S
Time per source (minutes)	1.75
FWHM primary beam ($\sim 1.13\lambda/D$)($''$)	22
Proj. baseline range (kλ)	10-808
Resolution ($''$)	0.3
Maximum Recoverable Scale[b]($''$)	3.0
Sky Frequency (GHz)	233
Spectral Window Center Freqs. (GHz)	224, 226, 240, 242
Channel width (MHz)	15.625
Channels per Spectral Window	128
Effective Total bandwidth (GHz)	7
Flux calibrator	J1751+0939
Bandpass calibrator	J1751+0939
Gain calibrator	J1824+0119

which was scheduled with 3 unequal scans) totalling $\sim$ 2 minutes on source. Automatic data flagging and flux, gain, and water vapour calibration were applied to the raw visibility data using the ALMA pipeline in version 4.5.3 of the Common Astronomy Software Applications (CASA) package[1] (McMullin et al., 2007). In addition to the full reduction, two subsets of the data were created using only the calibrated science target visibilities from either the first or second scan (excluding Ser-emb 5) in order to estimate the detectable lower limits for flux variations for future ALMA observations (see chapter 3). Phase-only self-calibration using the CASA `gaincal` task was attempted for every science target in the full data set and each single scan subset. Where successful, self-calibration was repeated 2-3 times with successively smaller solution intervals ranging from the scan duration to the integration time for each visibility. For the brighter targets, self-calibration provided an improvement of up to 30 % in SNR.

[1] Available at http://casa.nrao.edu

2.2 CARMA Observations and Calibration

Enoch et al. (2011) observed nine of the deeply embedded protostars in Serpens (table 2.1) at 230 GHz with CARMA, a 23 element interferometer with six 10.4 m, nine 6.1 m, and eight 3.5 m antennas. The targets were observed using the 10.4 m and 6.1 m antennas from 2007-2010 in CARMA's B, C, D, and E configurations to sample spatial scales from 51.6″-0.41″. While the maps of the sources produced by Enoch et al. (2011) combine data from all configurations across three years of observations, the goal is to search for variability on month-to year timescales, and thus individual *uv*-plane tracks (i.e., nights of observations) are focused on instead.

Each CARMA track samples a range of spatial frequencies in the uv-plane, which are determined by the (projected) baseline lengths of the array configuration. Ideally, the ALMA and CARMA observations would have similar *uv*-plane coverage so that the observations would be sensitive to similar spatial scales of the sky intensity, and images could produced and used to directly compare the observations. Owing to large differences in the CARMA and ALMA array configurations however, this is generally not the case. Figure 2.1 shows a comparison of the baselines length distribution in the CARMA B-E configurations and the ALMA configuration used. While there is significant overlap between CARMA B/C and ALMA, the CARMA D and E configurations only have baseline lengths overlapping with 10-20% of ALMA. Furthermore, the D and E configurations do not sample the spatial scales close to the effective photosphere where the signature of variability is strongest. While the ALMA data could still possibly be compared to the CARMA D and E data if most of the ALMA visibilities at large *uv*-distances were removed (see techniques of chapter 4), this would have resulted in at least a factor of 2-3 drop in the ALMA SNR, and thus this was not attempted

Although the CARMA B array tracks have *uv*-plane coverage very similar to the ALMA data, the quality of the data is degraded by worse weather conditions at the wetter CARMA site, and which in general are poorer for longer CARMA baselines (Zauderer et al., 2016). None of the science targets in single B-configuration tracks could be detected. Thus only the CARMA C-configuration data is used for this variability study (see sections 4.2-4.4).

Several nights of observations in the C-configuration were taken over $\sim$ 2 weeks in Fall 2007, the properties of which are summarized in table 2.3. Flux and bandpass calibrators were observed at the beginning or end of each observation followed

Table 2.3. CARMA C Configuration Observing Setup

Parameter	Value
Observation date(s)	Oct 24 2007 - Nov 05 2007
Number of Antennas	6×10.4 m + 8-9×6.1 m
Project code	cx190
Time per source (minutes)	60 - 90
FWHM primary beam[a](″)	28-47 (37.5)
Proj. baseline range (kλ)	13.2-25.4
Resolution (″) [b]	1.5
Maximum Recoverable Scale (″)	15.5
Sky Frequency (GHz)	230
Spectral Window Center Freqs. (GHz)	224.0, 224.5, 225.0, 229.5, 230.0, 230.5
Channel width (MHz)	31.25
Channels per Spectral Window	15
Total bandwidth (GHz)	2.8125
Flux calibrator(s)	MWC349, 3C273, Neptune
Bandpass calibrator	J1751+096
Gain calibrator	J1751+096

[a]CARMA's primary beam size varies depending on the combination of 10.4 m and 6.1 m antennas used in a baseline. The range from the smallest to largest primary beam sizes is given, and the FWHM of the primary beam that results when data from all baselines is combined is shown in parentheses.

[b]The resolution listed here is lower than the value calculated from the maximum projected uv-distance due to significant flagging of longer CARMA baselines.

by interlaced science and gain calibrator observations. Each track targeted three or four sources for 3-8 hours around transit (table 2.4). Integration times varied between sources depending on the expected flux from single dish observations. The archived raw data were obtained and manually calibrated using the MIRIAD data reduction package (Sault et al., 1995). Once calibration was accomplished, the data were converted to the CASA measurement set format using the `importmiriad` task, and further processing and imaging of the data were carried out in CASA.

2.3 Reduced ALMA Maps and Source Identification

Maps of the Serpens protostars targeted by the ALMA observations were produced using the `clean` task in CASA 4.7.2. During self-calibration, all channels in each

Table 2.4. CARMA C Configuration Tracks and Sources Observed

Field	Track Name			
	C1.2	C1.5	C1.8	C2.3
Track Length (min)	167	315	287	471
All fields	3	3	1	4
Ser-emb 1	1	1	1	-
Ser-emb 2	-	-	-	-
Ser-emb 3	-	-	-	-
Ser-emb 4	0	0	0	-
Ser-emb 5	0	0	0	-
Ser-emb 6	2	2	-	-
Ser-emb 7	-	-	0	0
Ser-emb 8	-	-	-	-
Ser-emb 9	-	-	-	-
Ser-emb 15	-	-	-	1
Ser-emb 11/17[a]	-	-	-	3

Note. — 0 = undetected, - = unobserved by this track. Note that although Ser-emb 8 was observed at 230 Ghz by Enoch et al. (2011), it was never observed using the C configuration. There is data in the archive for two additional tracks, C1.9 and C1.10, however, they are cut short by degrading weather and no sources can be detected.

[a]Observed as a 7-pointing mosaic encompassing both sources.

Table 2.5. ALMA Sources

ID	Field Ser-emb #	Position RA, Dec (ICRS)	Peak Flux (mJy beam^{-1})	Total Flux Density (mJy)	Deconvolved Size[a] (arcsec)	RMS (mJy beam^{-1})	Position Angle (degrees)
1	1	18:29:09.09 +00:31:30.9	92.64 (0.88)	125.37 (1.90)	0.24 x 0.14	0.20	98
2	2	18:29:52.53 +00:36:11.5	7.41 (0.30)	18.95 (1.05)	0.63 x 0.11	0.06	165
3	2	18:29:52.54 +00:36:10.3	0.97 (0.30)	0.96 (0.51)	-	0.06	-
4	2	18:29:52.40 +00:35:52.6	8.66 (0.31)	23.85 (1.12)	0.59 x 0.26	0.06	53
5	3	18:28:54.87 +00:29:52.0	9.10 (0.18)	10.54 (0.35)	0.15 x 0.09	0.07	151
6	4 (N)	18:29:59.94 +01:13:11.3	2.80 (0.11)	3.66 (0.24)	0.22 x 0.12	0.07	51
7	4 (N)	18:30:00.67 +01:13:00.1	3.16 (0.11)	3.50 (0.21)	0.13 x 0.07	0.07	68
8	4 (N)	18:30:00.73 +01:12:56.2	3.14 (0.11)	3.43 (0.20)	0.12 x 0.06	0.07	131
9	5	18:28:54.91 +00:18:32.3	7.85 (0.09)	10.08 (0.19)	0.19 x 0.12	0.07	162
10[b]	6	18:29:49.80 +01:15:20.3	342.46 (5.35)	985.14 (20.05)	0.45 x 0.40	0.67	165
11[b]	6	18:29:49.66 +01:15:21.1	29.33 (4.98)	119.72 (24.85)	0.68 x 0.45	0.67	88
12	7	18:28:54.06 +00:29:29.3	16.75 (1.02)	22.12 (2.16)	0.20 x 0.16	0.08	77
13	8	18:29:48.72 +01:16:55.5	15.19 (1.48)	37.28 (4.92)	0.48 x 0.29	0.13	69
14	8	18:29:48.09 +01:16:43.3	28.81 (1.51)	53.18 (4.04)	0.33 x 0.24	0.13	35
15	9	18:28:55.82 +00:29:44.3	3.34 (0.20)	5.07 (0.47)	0.29 x 0.17	0.07	99
16	9	18:28:55.77 +00:29:44.1	3.14 (0.21)	5.35 (0.52)	0.29 x 0.23	0.07	48
17	11 (W)	18:29:06.62 +00:30:33.9	30.77 (0.54)	57.20 (1.45)	0.30 x 0.28	0.14	87
18	11 (W)	18:29:06.77 +00:30:34.1	16.35 (0.52)	20.89 (1.08)	0.19 x 0.13	0.14	163
19	11 (W)	18:29:07.09 +00:30:43.0	3.03 (0.47)	2.49 (0.72)	-	0.14	-
20	15	18:29:54.30 +00:36:00.7	34.58 (0.53)	61.48 (1.40)	0.41 x 0.15	0.07	117
21	17	18:29:06.20 +00:30:43.0	41.48 (0.62)	97.87 (2.00)	0.38 x 0.35	0.12	138
22	17	18:29:05.61 +00:30:34.8	7.17 (0.58)	7.76 (1.07)	0.11 x 0.06	0.12	165

[a]A "-" in the deconvolved size column indicates the source is un-resolved.

[b]Associated with SMM1

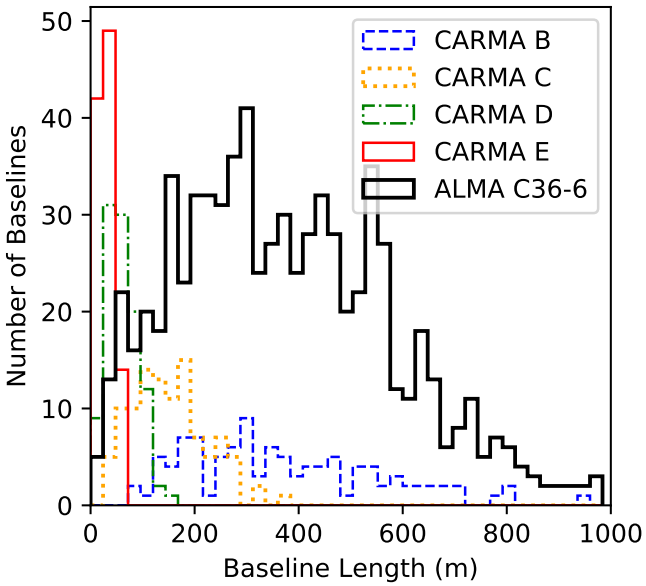

Figure 2.1 Baseline length distributions for four CARMA configurations and the ALMA configuration used for. Each bin is 24m wide.

spectral window were averaged together to increase the SNR. The `clean` task was then run in multi-frequency synthesis mode to a threshold of 3σ (measured by the RMS in an emission free region of each image) using Briggs weighting with robust=0.25 and a pixel size of 0.06″ to produce 60x60″ maps. All maps were primary beam corrected before measuring the flux of point-like sources by Gaussian fitting. Postage stamps from the resulting maps are shown in figures 2.2 and 2.3, while the corresponding Gaussian fits are provided in table 2.5. In each figure, YSOs previously identified by mid-IR Spitzer surveys (Dunham et al., 2015) are indicated by green pluses (Class 0, I, and Flat-Spectrum) and orange crosses (Class II and III).

While Enoch et al. (2011) only detected sources towards nine of the twelve Serpens fields surveyed, the ALMA observations find sources in every field owing to ALMA's higher sensitivity (0.1 mJy vs the $>$ 0.9 mJy in the CARMA maps). Most sources are resolved by the 0.3″ beam, and many are surrounded by extended structure which may in some cases be evidence of cavity walls sculpted by outflows. As the ALMA configuration used was selected to filter out spatial scales larger than 3.0″, there is additional extended structure missing from the images. Ser-emb 4 (N) shows a clear example of this, as it is faint and marginally resolved out by ALMA, but is strongly detected (SNR $>$ 20) in CARMA maps made only with visibilities for scales $>$ 4.1″ (Enoch et al., 2011).

In comparisons to the locations of the ALMA sources with Spitzer YSOs, there is generally good correspondence, however, there are several sources detected in the 1.3 mm maps with no associated Spitzer source. Discussion of these sources and further descriptions of each ALMA map are given in the appendix.

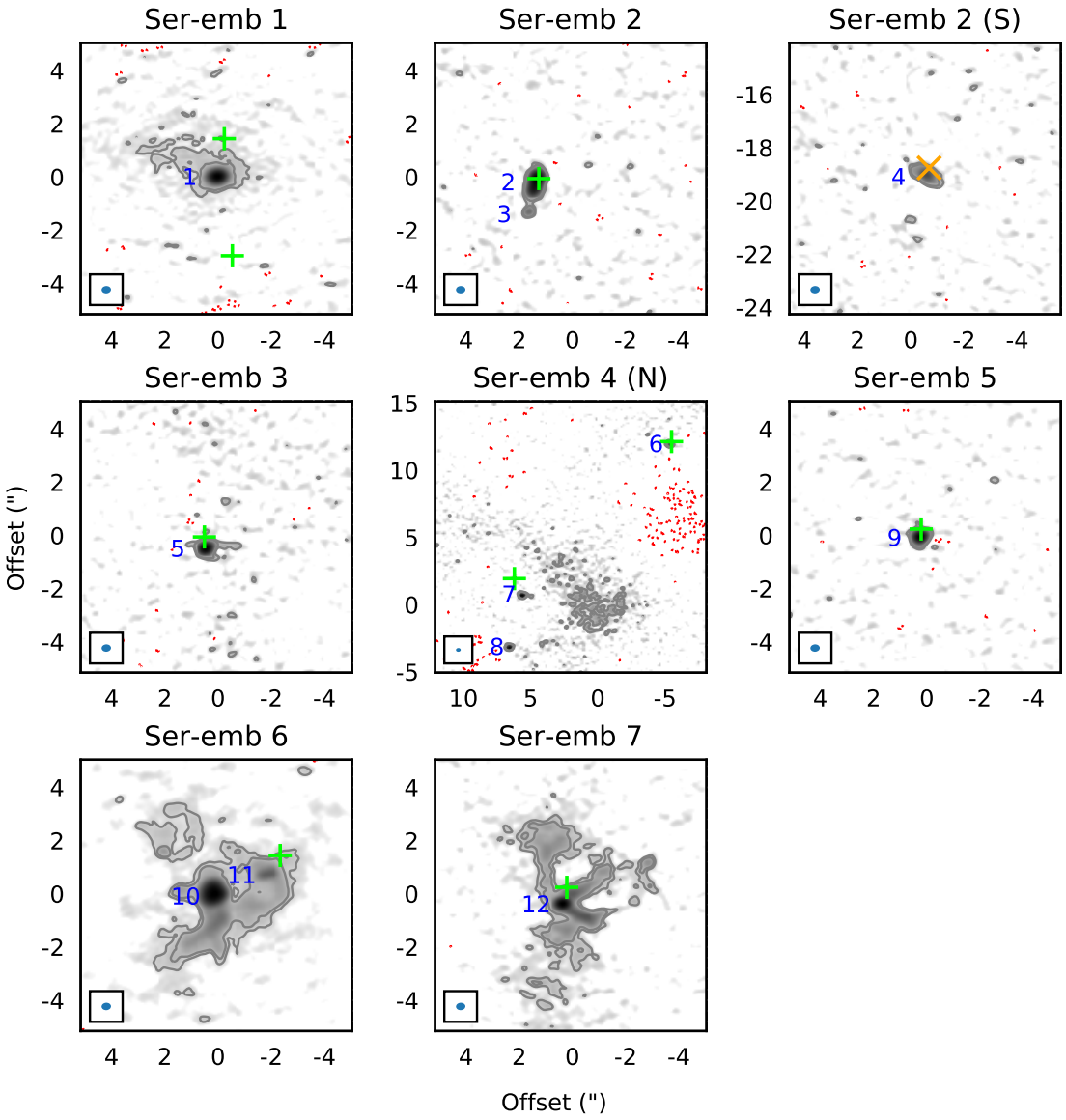

Figure 2.2 Postage stamps from the ALMA maps of the Serpens Sample of deeply embedded protostars. Intensity is shown in negative greyscale with logarithmic scaling to highlight extended structure. The x and y axes correspond to the offset from the pointing center (table 2.2) of each map. Grey contours are shown at 3 and 5 times the RMS in each map, while dashed red contours are shown at -3 times the RMS. Blue numbers indicate the ID of the sources in each map which were fit by a Gaussian in table 2.5. YSOs previously identified by mid-IR Spitzer (Dunham et al., 2015) surveys are indicated by green pluses (Class 0+I and Flat Spectrum) and orange crosses (Class II and III). Each map is shown without primary beam correction for clearer flux scaling. Full maps from each pointing are provided in the appendix.

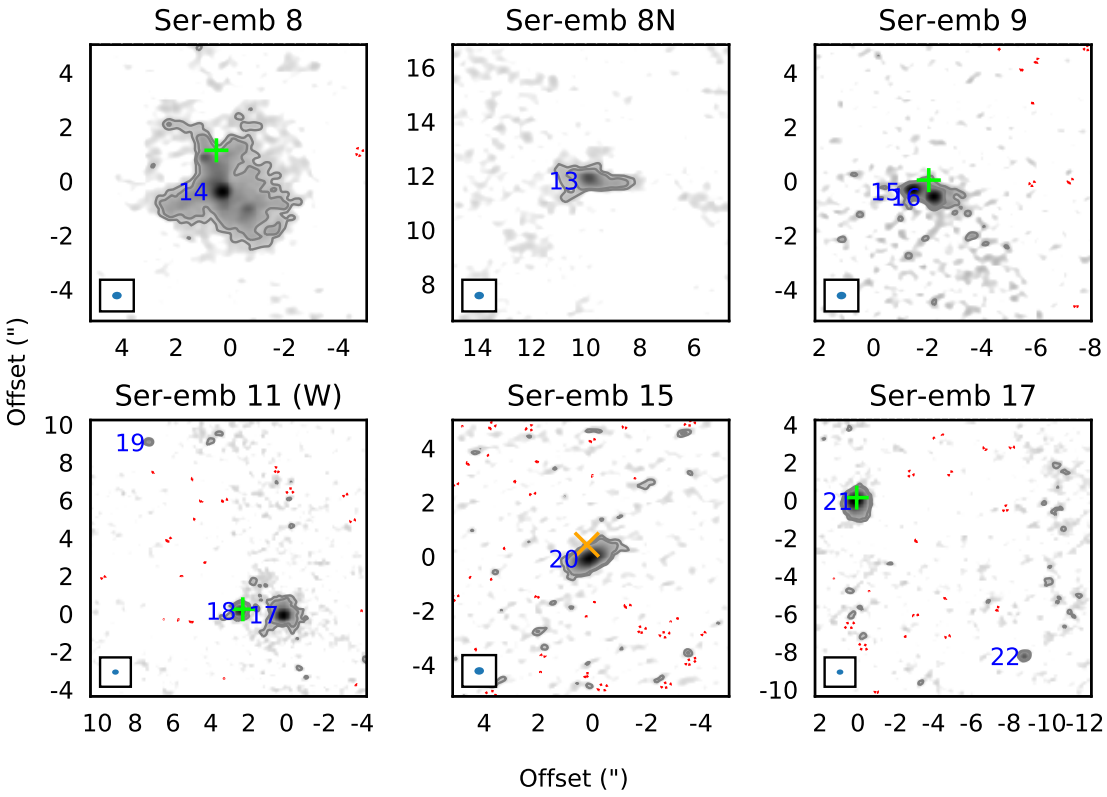

Figure 2.3 Figure 2.2 cont.

Chapter 3

Detecting Variability in Ideal Comparisons of Interferometer Observations

The smallest variation in flux of a source that can be robustly detected by comparing two interferometric observations depends upon the continuum RMS noise, the method used for calibrating and measuring flux, and how differences in spatial and spectral configurations are accounted for. The most ideal situation would be the comparison of observations made with the same telescope and identical setups, and thus here the 2016 observations are compared against themselves to find approximate lower limits on detectable flux variations, while discussion of comparing different interferometer setups is left to chapter 4.

3.1 Continuum RMS Noise of Observations

Our 2016 ALMA observations were requested to reach a continuum RMS noise level of 0.1 mJy, defined as the RMS in an emission free region of a deconvolved (i.e. cleaned) continuum image. This RMS noise limit was intended to allow reaching a SNR > 50 for the targets, where the SNR is defined as the ratio of peak flux[1] to RMS noise.

For the ALMA maps produced from the first scan, the achieved RMS noise (and the RMS as a percentage of the peak flux) is plotted against the peak flux for each source in figure 3.1. Many of the detected sources have an RMS noise greater than that expected (i.e., above $\sqrt{2}$ times the red curve), however, this can be readily explained by the reduced sensitivity of the ALMA dishes to sources near the edge of the field of view and the dynamic range limit of ALMA. Large open symbols in figure 3.1

[1]Peak Flux is somewhat of a misnomer, as its units are actually those of intensity (e.g. Jy/beam). However, for a point source the flux in a beam is exactly the same as the total flux, and the term "Peak Flux" is reasonable.

account for the increased noise for sources nearer the edge of the field of view, while smaller filled symbols indicate the RMS noise level had every source been at the field center. Some sources still would lie significantly above the expected noise level even if they had been observed at the field center (small grey symbols). Here the noise is dominated by the dynamic range limit of ALMA due to a brighter source in the same field (green symbols). ALMA's dynamic range limit describes the expected SNR for the brightest source in the field without self-calibration, and is nominally 100 for Band 6 observations (ALMA Cycle 3 Proposer's Guide). We find through a fit to the expected noise behaviour for the observations after self-calibration (blue curve in figure 3.1.) that the dynamic range limit is ~ 400.

3.2 Comparison of First and Second ALMA Scans

To estimate lower limits on detectable flux variations using only ALMA, the visibility data for each field was divided into its individual scans, then independently self-calibrated and imaged each scan using the same `CASA clean` parameters as those for the full data set in section 2.3. Integrated and peak fluxes were measured for each source by an elliptical Gaussian fit using `CASA imfit`. We also measured the integrated and peak flux in fixed regions of the sky enclosing each source ("Box Method"), typically a square 1-1.5″ in size. For this method, the uncertainty in the peak flux is the RMS noise, while that for the integrated flux is $\sqrt{N}$ times the RMS noise, where N is the number of pixels in the region. The use of the Box Method for measuring flux is motivated by the large number of sources which are resolved and/or embedded in extended structure, and therefore not well described by a Gaussian model.

Regardless of how flux measurements are made on the images, direct comparisons between two ALMA observations will be limited by the nominal Band 6 flux calibration accuracy of ∼10% (ALMA Cycle 3 Technical Handbook). Poor flux calibration accuracy is a general issue with mm/sub-mm observing caused by the paucity of bright, stable point sources [2].

To sidestep this problem, one can turn to relative flux calibration methods similar to those used in the JCMT Transient Survey (Mairs et al., 2017a), and apply them to both the predictions here and the comparison of ALMA and CARMA observations

[2] mm/sub-mm observations are most often calibrated using bright quasars, or if available, solar system planets. Unfortunately, Quasars are highly variable at these wavelengths, while planets are typically resolved and require very accurate flux models.

in chapter 4. We determine Relative Flux Calibration Factors (rFCFs) to bring the flux scale of the first scan into agreement with the second by fitting an average to the flux ratios between scans for bright sources (> 10 mJy or mJy/beam)[3]. We also separately find rFCFs for only the dim sources (< 10 mJy or mJy/beam) as a sanity check and to see what level of variability could be detected without bright sources. When fitting the average to determine the rFCF, each point is weighted by σ^{-2}, where σ is the uncertainty in the ratio given by the errors added in quadrature of the flux measurements in the first and second scan. The overall uncertainty in the rFCF is given by the standard deviation of the ratios, again weighted by σ^{-2}.

The ratios and rFCF fits for just the Box peak flux and Gaussian integrated flux are shown in figure 3.2, while table 3.1 summarizes all rFCF values. All of the rFCFs are consistent with 1, and most deviate by $\lesssim 0.01$, demonstrating that the ALMA calibration is extremely stable between scans on the ~ 40 minute timescale of the observations. The precision of rFCFs derived from integrated fluxes are typically lower than those derived from peak fluxes by a factor of 2-5, due to the larger relative uncertainties in integrated flux. The precision for rFCFs determined using Gaussian fits are lower than those using the peak/integrated Box flux because the flux measurements are assumed to be independent between scans, yet many of the sources are poorly described by a Gaussian model and thus have flux uncertainties dominated by the quality of fit. This causes the flux uncertainties to be correlated scan-to-scan, resulting in a larger rFCF uncertainty. The best rFCF precision is thus achieved using the Box peak flux (essentially the SNR), with a precision of 0.7% and 3.3% for bright and dim sources respectively. This is consistent with what would be expected from the inverse of the SNR for representative dim (~ 30) and bright ($\gtrsim 100$) sources.

It should be emphasized that reaching sensitivity to low levels of variability requires both a precisely determined rFCF *and* high SNR flux measurement for an individual source. Table 3.2 summarizes the percentage change in flux the observations would be sensitive to at a 3σ level for a given rFCF and Flux percentage error (assuming that the Flux percentage error does not change between observations). Using the Box peak flux rFCFs, the ALMA observations are thus sensitive to variability at the $\sim 16\%$ level for representative dim sources (3 mJy; 3% flux error) and at the $\sim 4.8\%$ level for bright sources (10 mJy; 1% flux error).

[3]At the requested 100 μJy RMS noise of the observations, the bright sources are those for which reach the desired SNR > 100.

Table 3.1. Relative Flux Calibration Factors (rFCFs) for ALMA data

rFCF Measurement Method	Dim	Bright
Box Peak Flux	1.006 (0.033)	0.998 (0.007)
Box Int Flux	0.990 (0.152)	0.997 (0.012)
Gaussian Peak Flux	1.012 (0.074)	1.002 (0.012)
Gaussian Int Flux	1.031 (0.138)	0.995 (0.038)

Table 3.2. 3σ Percentage Variability detection Thresholds

Flux Err. (%)	rFCF Err. (%)						
	0.3	0.5	1	3	5	10	20
0.3	1.6	2.0	3.3	9.1	15.1	30.0	60.0
0.5	2.3	2.6	3.7	9.2	15.1	30.1	60.0
1	4.3	4.5	5.2	9.9	15.6	30.3	60.1
3	12.8	12.8	13.1	15.6	19.7	32.6	61.3
5	21.2	21.3	21.4	23.0	26.0	36.7	63.6
10	42.4	42.5	42.5	43.4	45.0	52.0	73.5
20	84.9	84.9	84.9	85.3	86.2	90.0	103.9

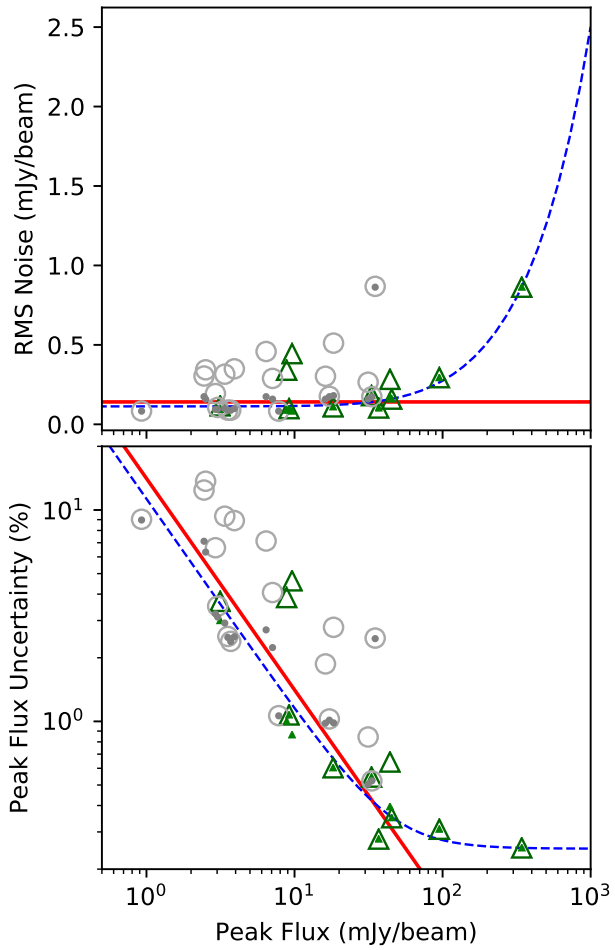

Figure 3.1 Upper panel: Achieved RMS noise vs the peak flux for each source in the first scan of the ALMA observations. Lower panel: Same as upper panel, but with the % uncertainty in Peak Flux on the y axis, i.e., the RMS noise divided by the Peak Flux. Large open symbols represent measurements accounting for the increased noise due to the reduced sensitivity of the ALMA primary beam near the field edge, while small filled symbols use the RMS noise at the field center. Green triangles are the brightest sources in a given field, grey circles are from fields with a brighter source, which may cause ALMA to reach its dynamic range limit. The red line is $\sqrt{2}$ times the requested RMS noise of 0.1 mJy. The blue curve in the upper panel is an empirical fit to the brightest peaks with the RMS noise of the field center of the form $A = \sqrt{R^2 + P^2/D^2}$, where A and R are the achieved and requested RMS, P is the peak flux, and D is the fitted dynamic range limit. The blue curve in the lower panel plots this function divided by Peak Flux, A/P.

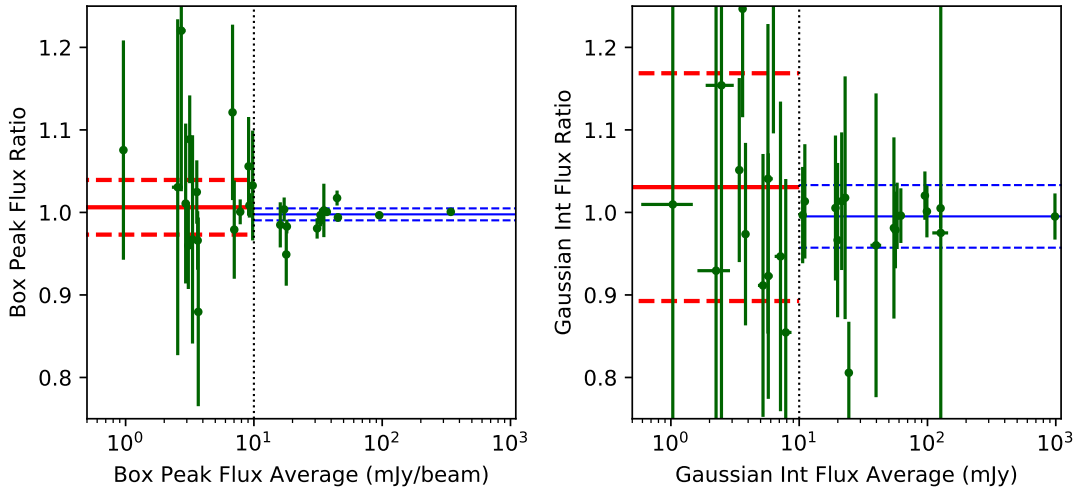

Figure 3.2 Ratio between the second and first scans in peak flux estimated using a fixed region (box) on the sky and integrated flux estimated by a Gaussian fit. The average weighted by σ^{-2} and the associated standard deviation are shown by the solid and dashed lines for dim sources (< 10 mJy or mJy/beam), and bright sources (> 10 mJy or mJy/beam). The values of these averages are summarized in table 3.1

.

Chapter 4

Detecting Variability between Distinct Interferometric Observations with ALMA and CARMA

While the results of chapter 3 provide a lower limit for detections of variability in the most ideal conditions, they do not take into account the complications involved in comparing typical interferometric observations. These issues are caused by the inherent flexibility of interferometers, which typically have multiple array configurations for recovering structure over a range of spatial scales, and a variety of frequency bands and correlator modes for sampling different parts of the spectrum.

For comparing the ALMA and CARMA observations, the problems caused by differences in array configuration are first addressed in sections 4.1-4.3, and relative flux calibration methods are explored to search for variability in section 4.4.

4.1 Impact of Differences in Spatial Configurations

Interferometers sample the complex visibility $V(u, v)$ of a source, a Fourier transform of its intensity distribution on the sky (ignoring effects of the primary beam) and a function of the spatial frequencies u and v. The spatial frequencies sampled are determined by the projected lengths of the array's baselines (in units of the observing λ) on the sky in the East-West (u) and North-South (v) directions. Since the projected baseline lengths and orientations change as the earth rotates, the uv-plane becomes better sampled over the course of observation, however, this implies that no two interferometric observations will recover exactly the same visibilities unless they observe with identical array configurations and observing schedules, from the same latitude, and at the same wavelength. Since the synthesized beam is simply

the Fourier transform of the (weighted) visibility sampling function, this is equivalent to stating that two observations will not have the same beam unless subject to the above conditions.

While differences in uv-plane sampling are not a problem for imaging point sources, (which have a constant visibility amplitude over the uv-plane) images of resolved sources constructed by inverting $V(u, v)$ will contain varying amounts of flux depending on the uv-plane sampling. This issue is partly mitigated by algorithms used in imaging such as CLEAN, which effectively estimate $V(u, v)$ in un-sampled regions of the uv-plane by interpolating between samples, however, extrapolating to regions with no samples at all is extremely difficult. In particular, CLEAN has trouble in accurately extrapolating to the center of the uv-plane (where large spatial scales are measured), which is typically poorly sampled by interferometers because of a lack of short baselines.

An example is helpful in further illustrating how differences in uv-plane sampling can affect the recovered flux. Consider a point source embedded in extended structure observed by two different configurations of the same interferometer - the first with the antennas in a group compact enough to recover the largest spatial scales of the extended structure, and the second with the antennas spaced further apart, providing higher resolution but missing some of the extended structure. If images are produced for both observations and the flux of the point source is to be measured, the compact configuration image can be used to make a more accurate estimate of the point source flux by fitting for both the point source and the underlying larger scale structure.

To account for this bias, changes in the flux of this point source between the two observations should be measured using images constructed only using visibilities which measure similar spatial scales. There are several ways to accomplish this which are discussed in the following sections, including uv-plane matching of synthesized beams and simulated observations.

4.2 uv-plane Matching of ALMA and CARMA Synthesized Beams

To directly compare the ALMA and CARMA data for a given source, only visibilities from each observation which sample a similar region of the uv-plane are included, in order to match the synthesized beam shapes as closely as possible. This requires some care, as a simple euclidean distance is not appropriate for comparing uv-plane separations between visibilities. The angular scale a visibility measures is the inverse

of its euclidean distance from the uv-plane origin, and thus a given euclidean distance between two points near the origin is equivalent to a much larger change in angular scale than for the same distance between two points far from the origin. To avoid this problem, the euclidean distance between ALMA and CARMA visibilities as a *fraction* of the uv-distance to the CARMA visibility from the origin is used instead. Figure 4.1 shows in detail how this fractional distance is used for matching two fictional ALMA and CARMA data sets with an unrealistically large cutoff distance of $f_{\text{cut}} = 0.4$.

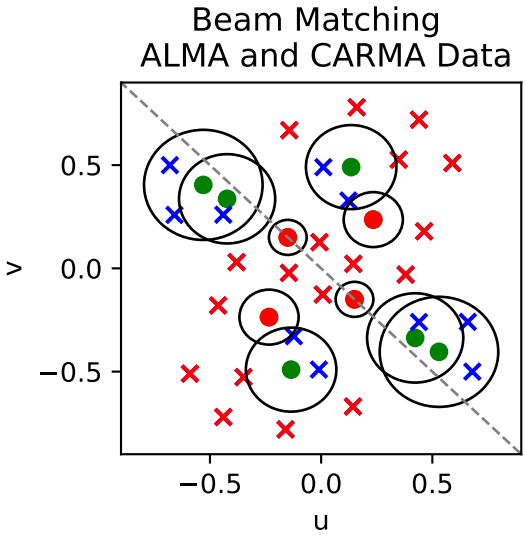

Figure 4.1 Demonstration of how beams are matched for the observations using two fictitious data sets. ALMA and CARMA visibilities in the uv-plane are indicated by blue/red crosses and green/red disks respectively. Red disks and crosses are visibilities which will be removed from each data set by beam matching. The dashed grey line shows the inherent symmetry axis of the uv-plane. The black circles around each CARMA visibility indicate the cut-off distance for beam matching; if there are no samples from the ALMA data set within the cut-off distance (here, $f_{\text{cut}} = 0.4$), the CARMA visibility in the original data set is removed. Any ALMA visibilities which do not fall within the cut-off distance to a CARMA visibility are also removed.

For comparisons of the observations, the value of f_{cut} should be optimized by choosing it to match the beam dimensions as closely as possible (smaller f_{cut}) without removing so much data that the SNR drops severely (larger f_{cut}). Since the distribution of baselines for the ALMA configuration is essentially a superset of those for CARMA C (see figure 2.1), a useful value of f_{cut} should mostly remove visibilities from the ALMA data while retaining as many from the (much lower SNR) CARMA data as possible. Figure 4.3 shows the distributions of nearest neighbours between

a pair of ALMA and CARMA observations of the same Serpens source in units of fractional distance, from which a value of $f_{\rm cut}$ of ~ 0.25 appears optimal. Since the *uv*-coverage is similar for all other pairs of observations, $f_{\rm cut} = 0.25$ is used in every comparison. Figure 4.2 shows an example of the *uv*-plane distributions before and after applying beam matching with $f_{\rm cut} = 0.25$ to a pair of ALMA and CARMA observations of the same source.

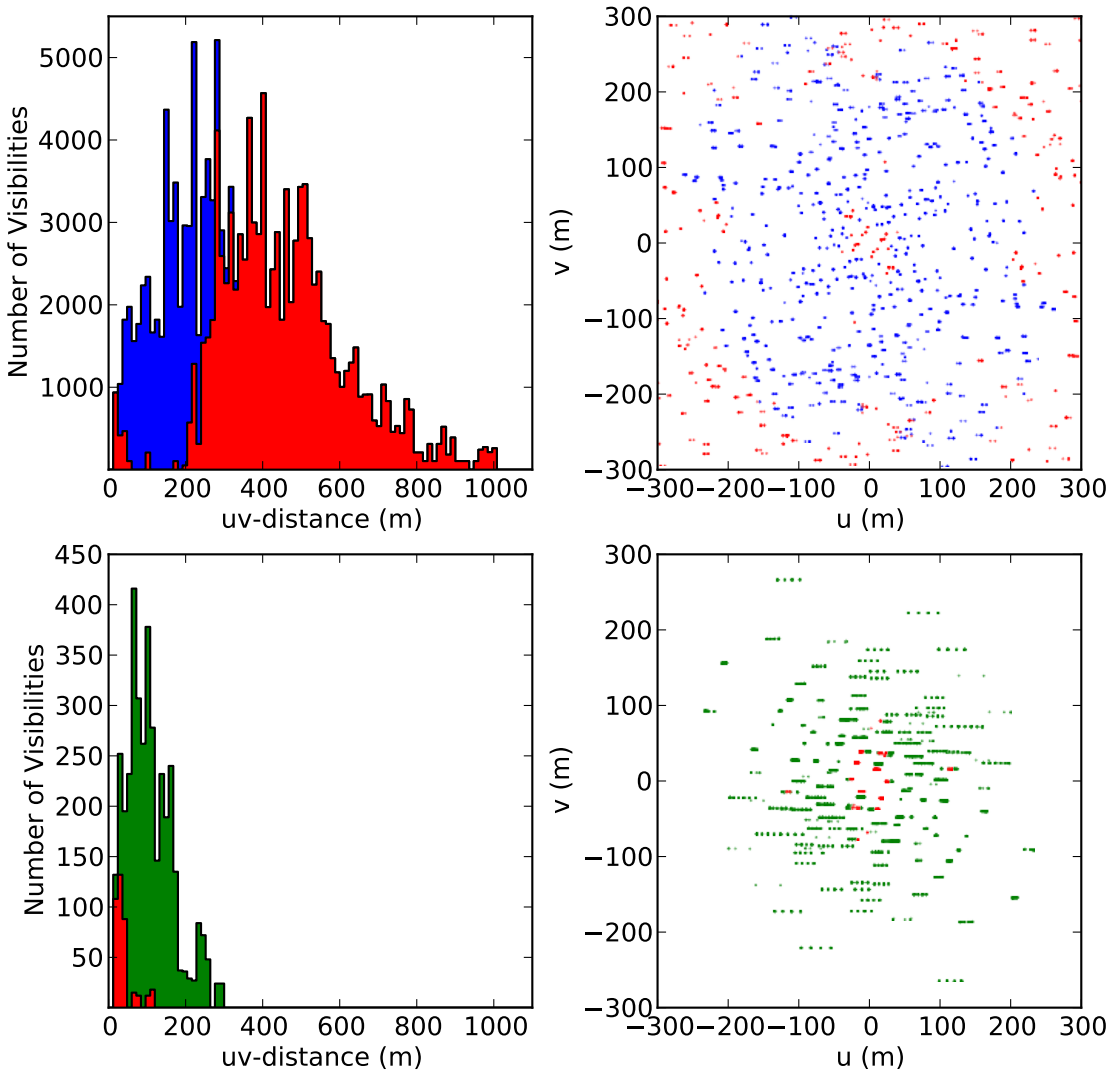

Figure 4.2 Effect of applying beam matching with $f_{\rm cut} = 0.25$ on the *uv*-plane distributions of visibilities for CARMA Track C1.2 and the ALMA observations of Ser-emb 1. The top and bottom rows of panels shows the ALMA and CARMA distributions respectively, where red indicates visibilities removed by beam matching.

Once the visibility data from each observation to be compared are selected, pre-

liminary maps are produced with the same parameters as for the full ALMA maps in section 2.3. In table 4.1, the beam shapes before and after matching are compared. While correspondence in the ALMA and CARMA synthesized beams has improved with their respective increase and decrease in size, CARMA's beam is still typically $\sim 0.3''$ larger in either axis than ALMA's. This can be attributed to differences in the uv-plane sampling density and weighting of the visibilities which uv-plane matching does not take into account. The sampling density of ALMA is significantly better than CARMA at all uv-distances, but is relatively skewed towards large uv-distance owing to the longer baselines. Furthermore, longer baseline tend to also have larger phase scatter from atmospheric fluctuations, resulting in a drop in visibility amplitude (Zauderer et al., 2016). These noisier visibilities are flagged or given a lower weight during calibration, resulting in less sensitivity on longer baselines. This affects the data from CARMA more than that from ALMA because of the poorer observing conditions at the CARMA site. To correct for these effects, a uv-taper is also applied to each ALMA observation when imaging the data (last column of table 4.1). The taper used is equivalent to smoothing by a circular Gaussian kernel with FWHM equal to the major axis of the corresponding matched CARMA beam, and improves the agreement in beam shapes to within $\sim 0.1''$ or better for both axes.

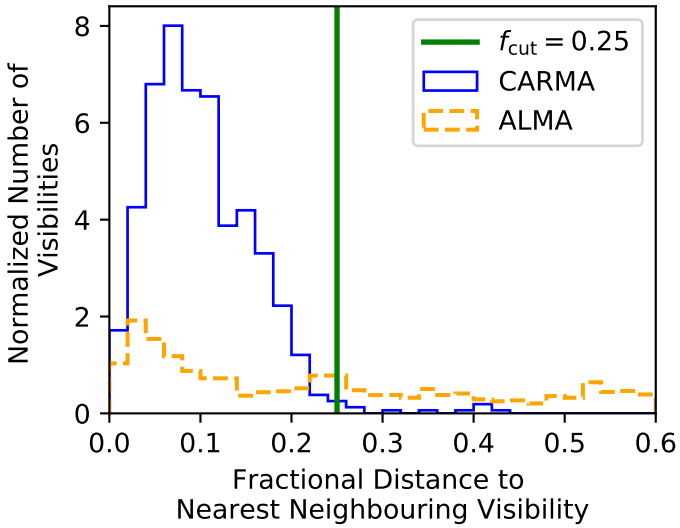

Figure 4.3 Normalized histograms of nearest neighbouring visibilities (in the other data set) for the ALMA and CARMA track C1.5 observations of Ser-emb 6. The bin size is 0.02. The fractional distance cut-off $f_{\rm cut}$ used for beam matching of all ALMA and CARMA observations is shown by the vertical line.

Table 4.1. Beam Shapes Before and After *uv*-plane Matching

Matching Track[a]	Unmatched (″)		Matched (″)		
	CARMA	ALMA	CARMA	ALMA	ALMA + *uv* taper
C1.2	1.73 x 1.40	0.35 x 0.27	1.16 x 1.00	0.82 x 0.65	1.19 x 1.02
C1.5	1.72 x 1.62		1.46 x 1.21	1.12 x 0.95	1.53 x 1.38
C1.8	1.67 x 1.43		1.30 x 0.85	0.92 x 0.54	1.32 x 1.10
C2.3	1.54 x 1.39		1.02 x 0.82	0.69 x 0.49	1.04 x 0.87

Note. — Beam sizes given are the FWHM of the major and minor axes.

[a] Since the *uv*-coverage for each source within an observation is nearly identical, we only compare the beams for one source observed by both.

4.3 Simulated Re-observations of ALMA sources with CARMA

Simulated observations provide another means of comparing the ALMA and CARMA data while taking into account differences in *uv*-plane sampling. Typically, simulated observations are used to predict what an interferometer will see with a particular array configuration and observing setup given a model of the true sky brightness. The model is often the result of a numerical simulation or an image from another telescope. In the present case, maps derived from the ALMA observations in section 2.3 with the residuals subtracted are used as models, and CASA's `simobserve` task is then used to simulate what CARMA would see had it re-observed the same sources in a identical manner as it did in 2007. The simulated images produced are compared against the beam matched CARMA maps from section 4.2. A similar approach was successfully used by Hunter et al. (2017) for detecting variability between SMA and ALMA observations of the massive protocluster NGC 6334-I, albeit with a readily detectable factor of ~ 4 change in flux.

In order to realistically simulate the conditions under which the original CARMA data were taken, the same array configuration, correlator setup, observing schedule, and data flagging must be used. For the simulated re-observations, the *uv*-coverage is ensured to be the same by extracting the exact positions of the CARMA antennas from the data and applying the same observing schedule, integration time, and flagging. For the spectral setup, a single 2.8 GHz wide spectral window centred on the ALMA observing frequency (227 GHz) is used instead of the exact parameters in table 2.3 due to limitations of the CASA `simobserve` task. While the observing frequencies of ALMA and CARMA are slightly different, changes in the flux should be small and mitigated by relative flux calibration (see discussion in chapter 5). Finally, no simulated thermal noise is added to the simulated visibilities, as only the differences in *uv*-coverage that would affect measurement of variability are being modelled, and the present goal is not to determine sensitivities for a CARMA to CARMA comparison.

From the simulated visibilities, maps are produced using the same parameters as those in section 2.3, but only including visibilities more than 30m from the *uv*-plane origin. This *uv*-plane cut is applied as a good approximation to the effects of beam matching on the CARMA data[1]. The simulated and *uv*-plane matched beam shapes are compared against each other in table 4.2. As was similarly the case for beam

[1]This also ensures that the simulated CARMA maps do not contain larger spatial scales than the ALMA observations used as models (with relatively fewer short baselines than the CARMA C configuration) were sensitive to.

Table 4.2. CARMA Beam Shapes In Real and Simulated Observations

Track	Matched (″)	Simulated (″)	Sim. + Taper (″)
C1.2	1.16 x 1.00	1.08 x 0.71	1.18 x 0.95
C1.5	1.46 x 1.21	1.23 x 1.06	1.44 x 1.25
C1.8	1.30 x 0.85	1.09 x 0.75	1.24 x 1.05
C2.3	1.02 x 0.82	0.89 x 0.77	1.02 x 0.92

Note. — Beam sizes given are the FWHM of the major and minor axes.

matching, differences in beam shape of $\sim 0.2''$ remain, however, this likely arises from variations in the visibility weighting not modelled in the simulations, as the *uv*-coverages of the beam matched and simulated observations are nearly identical. To correct for this, a *uv*-taper corresponding to the CARMA matched beam is added to each simulated image when cleaning as was done for beam matching.

4.4 Relative Flux Calibration Factors and Variability of Sources

With differences in beam shapes minimized, fluxes of sources common to both observations can be reliably measured and searches for variability may be attempted. As discussed in chapter 3, direct comparisons are limited by the nominal accuracy of the absolute flux calibration for each telescope, ∼10% for ALMA in Band 6 (ALMA Cycle 3 Technical Handbook) and ∼15% for CARMA (CARMA Memorandum 59). rFCFs are therefore calculated by fitting an average to the ratio of ALMA to CARMA Box peak fluxes, and used to convert the CARMA maps to the ALMA flux scale for both methods of beam comparison. Specifically, rFCFs for *uv*-plane beam matching (section 4.2) are fit to the ratio of fluxes in pairs of beam matched CARMA and ALMA maps (specific to each CARMA track), while rFCFs for simulated re-observation (section 4.3) are fit to the ratio of fluxes between the ALMA maps with simulated re-observation by CARMA and the corresponding beam matched CARMA track. The resulting rFCFs for CARMA tracks C1.2, C1.5, and C2.3 and the standard deviation between them, σ_{rFCF}, are shown in table 4.3. Within the uncertainties given, differences in the flux calibration factors across beam comparison methods are

consistent with each other and reach a similar level of precision. Further comparison of the two methods and discussion of which may be best suited to future variability studies is given in chapter 5.

In table 4.3, a rFCF can not be properly calculated for CARMA track C1.8, as there is only a single observable source in common with the ALMA observations. Relative variability can thus not be detected, and the rFCF given is just the ratio of the brightness of this source (Ser-emb 1, ID 1). This ratio for C1.8 is consistent with the $\sigma_{\rm rFCF}$ found for the other three tracks.

Given that there is only one ALMA flux calibration for every image, $\sigma_{\rm rFCF}$ is effectively an estimate of the CARMA absolute flux calibration accuracy. $\sigma_{\rm rFCF}$ is found to be $\sim 40\%$ for either beam comparison method compared to the $\sim 15\%$ expected from the nominal CARMA absolute flux accuracy. Some of this loss of accuracy is probably caused by the low SNR of the sources used for relative calibration, and some might be attributed to poorer-than-average weather during several of the CARMA tracks. Since $\sigma_{\rm rFCF}$ was only determined from 3 tracks however, it is not particularly robust.

For tracks C1.2, C1.5, and C2.3, the rFCFs may be useful for measuring variability, but are still not particularly well constrained due to there only being 3-4 sources per track in common with our ALMA observations (see table 2.4). Determining accurate rFCFs is further hampered by the low signal to noise detections of many of the sources in the CARMA tracks, with most detected with a SNR of 5-15 and the brightest at a SNR of 30. For tracks C1.2 and C1.5, the relative flux calibration is good to the $\sim 10\%$ level, while for the fainter sources compared in C2.3, the relative flux calibration is accurate to $\sim 50\%$, no better than the $\sim 18\%$ uncertainty due to the combined absolute flux calibration of ALMA and CARMA.

Tables 4.4-4.6 compare the fluxes in each epoch for each track after application of the rFCFs. Here, the detection σ is the the percent difference between the fluxes divided by it's uncertainty. No source is seen to vary above $\gtrsim 1\sigma$ by either the beam matching or simulated observation analysis. The uncertainty in the percent difference for each source implies the ability to detect variability at a 3σ level is $\sim 24-60\%$ for tracks C1.2 and C1.5 and $\sim 75-180\%$ for track C2.3, depending on the brightness of the source in question. These detection thresholds are much larger than those expected from comparison of multiple epochs of ALMA data in chapter 3, emphasizing the need for large numbers of bright sources to achieve good sensitivity to variability.

Table 4.3. Relative Flux Calibration Factors

Beam Comparison Method	CARMA Track Name				$\sigma_{\rm rFCF}$
	C1.2	C1.5	C1.8[a]	C2.3	
Beam Matching	1.32 (0.09)	0.74 (0.11)	1.02 (0.06)	1.85 (0.54)	0.45
Simulated Re-Observation	1.15 (0.14)	0.64 (0.04)	0.93 (0.05)	1.56 (0.49)	0.37

[a]C1.8 Only has one source, Ser-emb 1 (ID 1), and the uncertainty of the rFCF has been replaced by the uncertainty in the ratio of the fluxes for this track. It is not included in the estimate for $\sigma_{\rm rFCF}$

Table 4.4. Variability of Sources, CARMA Track C1.2

Beam Comparison Method	ID	Beam Matched & Scaled CARMA Flux[a] (mJy beam^{-1})	Equivalent ALMA Flux (mJy beam^{-1})	Percent Difference	Detection σ
uv-plane Beam Matching	1	114.07 (16.31)	125.33 (0.69)	9.88 (15.72)	0.63
	10	876.38 (67.20)	847.56 (5.47)	-3.29 (7.44)	0.44
	11	121.95 (26.22)	113.91 (5.48)	-6.59 (20.58)	0.32
Simulated Re-Observation[b]	1	99.44 (17.58)	114.10 (0.02)	14.75 (20.28)	0.73
	10	763.97 (98.70)	773.80 (0.21)	1.29 (13.09)	0.10
	11	106.31 (25.39)	89.26 (0.21)	-16.03 (20.05)	0.80

[a]The flux for *uv*-plane Beam Matching and Simulated Re-observations differ only in the rFCF from table 4.3.

[b]The uncertainty in the Equivalent ALMA flux measurements with simulated re-observations is lower than in beam matching because the simulations do not include the effects of noise; see section 4.2

Table 4.5. Variability of Sources, CARMA Track C1.5

Beam Comparison Method	ID	Beam Matched & Scaled CARMA Flux[a] (mJy beam^{-1})	Equivalent ALMA Flux (mJy beam^{-1})	Percent Difference	Detection σ
uv-plane Beam Matching	1	155.20 (25.47)	129.80 (0.85)	-16.36 (13.74)	1.19
	10	966.61 (153.03)	919.68 (5.59)	-4.86 (15.07)	0.32
	11	187.46 (34.39)	227.24 (5.59)	21.22 (22.44)	0.95
Simulated Re-Observation[b]	1	134.89 (12.20)	120.83 (0.01)	-10.43 (8.10)	1.29
	10	840.12 (66.76)	860.11 (0.20)	2.38 (8.14)	0.29
	11	162.93 (19.90)	176.04 (0.20)	8.05 (13.19)	0.61

[a,b]See table 4.4.

Table 4.6. Variability of Sources, CARMA Track C2.3

Beam Comparison Method	ID	Beam Matched & Scaled CARMA Flux[a] (mJy beam^{-1})	Equivalent ALMA Flux (mJy beam^{-1})	Percent Difference	Detection σ
uv-plane Beam Matching	17	38.28 (14.75)	53.95 (0.23)	40.92 (54.29)	0.75
	18	34.14 (13.89)	21.38 (0.24)	-37.37 (25.50)	1.47
	20	68.42 (21.34)	57.52 (0.22)	-15.93 (26.22)	0.61
	21	78.10 (26.51)	87.77 (0.30)	12.38 (38.14)	0.32
Simulated Re-Observation[b]	17	32.21 (12.95)	47.75 (0.11)	48.25 (59.59)	0.81
	18	28.72 (12.14)	17.29 (0.11)	-39.79 (25.46)	1.56
	20	57.56 (19.13)	52.05 (0.01)	-9.58 (30.05)	0.32
	21	65.71 (23.54)	66.45 (0.15)	1.13 (36.23)	0.03

[a,b]See table 4.4.

Chapter 5

Discussion and Conclusions

Given that large bursts in deeply embedded protostars have only been detected a handful of times, the lack of flux variations above the detection limits of $\sim 24-180\%$ in the Serpens sample is not unexpected. The only source in the sample with prior evidence of variability is Ser-emb 6 (SMM1), which is rising by $\sim 5\%\mathrm{yr}^{-1}$ in the Transient Survey (Johnstone et al., 2018). Extrapolating over the 9 year difference between the ALMA and CARMA epochs and assuming a similar change would be seen (ignoring differences in spatial scale and observing frequency) suggests that a 45% increase in flux might have been expected, which would be at or above a 3σ detection level for this source (see tables 4.4-4.6). Given that variability is expected at the scales of the accretion disk, the signature of variability could be stronger than 45% in the comparisons of ALMA and CARMA observations, as in the Transient Survey changes in flux are diluted by additional cold envelope material in the JCMT beam. Instead, the results of section 4.4 are consistent with no change, suggesting that the rise in brightness of SMM1 seen by the Transient survey (between March 2016 and June 2017) may have only began recently.

The greatest limitations in the comparisons of the Serpens sample are imposed by the relatively low signal to noise of the CARMA data and the small numbers of objects common to both the ALMA and CARMA observations available for relative flux calibration, which hinder the determination of precise and statistically robust rFCFs. The comparisons of the ALMA data against itself however, suggest that if a second epoch with similar resolution and sensitivity were obtained, variations at the level of a few percent could be detected for sources with a SNR > 100, (those brighter than 10 mJy) about 14 in the sample. Moreover, ALMA's excellent sensitivity makes such an observation efficient - the ALMA snapshot observation reached a sensitivity of 100μ Jy in 40 minutes, compared to the sensitivity of the CARMA maps of 1-3 mJy

(Enoch et al., 2011), achieved by combining data from over 20 nights of observations over three years. As the JCMT Transient Survey finds 10% of protostars varying at $\sim |5|\%\mathrm{yr}^{-1}$, (including includes SMM1 (Ser-emb 6), an object also in the sample) a second epoch of ALMA observations with a similar array configuration and integration time would likely find robust low level variability in at least 1-2 objects. As the signature of variability is likely being diluted by the JCMT beam at the scales of the envelope it probes, it is possible that even more detections could be made.

The results of section 4 suggest *uv*-plane beam matching and simulated re-observations are similarly effective in terms of their sensitivity to variability, resulting rFCF precision, and ability to match the main lobes of the clean beams. While *uv*-plane beam matching is much simpler to implement, simulated re-observations can apply identical *uv*-plane sampling from one epoch of observations to the other by carefully taking into account the array setup. Both methods could possibly be improved by taking into account differences in visibility weighting between two epochs in a more precise way than the *uv*-tapering procedure chosen. Future work should also focus on generalizing these methods to compare > 2 epochs of observations, so reliable light curves can eventually be produced.

Some techniques not explored in this work could also improve the chances of finding variability. Small differences in observing frequency between the 233 GHz ALMA observations and 230 GHz CARMA observations have not been taken into account. Assuming a spectral index for optically thin dust of 2.5, a 3 GHz difference in frequency might see a difference in flux of 3.3%. The relative flux calibration should remove frequency dependent differences in dust emission in an average sense, but does not take into account variations in dust properties between objects. This can be corrected for by fitting a spectral index for each while performing deconvolution. This could be useful for comparing archival observations, which likely have been done with different observing frequencies as well as telescope configurations. Another unexplored technique is the possibility of *uv*-plane model fitting methods for measuring fluxes. These have the advantage of comparing the visibility data in the most direct way possible, but require a careful statistical analysis of how the visibility weighting affects the uncertainty in the flux measurement.

Future work on identifying variability in deeply embedded protostars is currently underway. An ALMA proposal for another epoch of observations on the Serpens sample in this work with the same resolution and sensitivity (PI: Doug Johnstone, project code `2017.1.00117.S`) may receive time in cycle 5 (October 2017 - September 2018),

providing an ideal second epoch for comparison. A Cycle 6 ALMA proposal for 4 epochs of Band 7 observations of variables in Serpens identified by the JCMT Transient survey has been accepted (PI: Logan Francis, project code `2018.1.00917.S`). This proposal uses only the Atacama Compact Array (ACA) component of ALMA, which consists of 10 7m antennas on 9 to 50m baselines and remains in a fixed configuration through cycle 6, significantly reducing differences in *uv*-plane sampling between epochs. These observations will complement results from the contemporaneous Transient Survey by observing at 850 μm with a resolution of 3.8″(compared to the 14.6″resolution of the JCMT), sufficient to reach the scale of the inner envelopes ($\sim$ 1500AU) of protostars in Serpens. Large scale far-IR maps of molecular clouds produced by upcoming flights of the Balloon-Borne Large-Aperture Submillimeter Telescope (BLAST) may provide the opportunity for a variability study at wavelengths much closer to the peak of the dust envelope SED, albeit at poorer resolution (25-50″). The combination of these new searches and the techniques and calibration issues discussed in this work ought to enable deeper connections between observations and current theoretical models of accretion in protostars.

Appendix A

ALMA Serpens Maps

The Serpens Main cluster has been extensively surveyed at a variety of wavelengths and resolutions over the past 30 years. The ALMA observations in this work provide some of the highest resolution and most sensitive maps of deeply embedded protostars in the cluster to date. In many of the targeted fields, single sources are thus resolved at the scale of the accretion disks, allowing significant extended structure to be uncovered and previously unknown faint sources to be identified. Here, each field is discussed the context of past and recent observations, and the positions of our sources are compared with YSOs identified in the Spitzer "cores to disks" (c2d) and "Gould Belt" (GB) surveys (Dunham et al., 2015). Table A.1 lists the properties of all c2d/GB YSOs in the ALMA fields associated with the mm sources in table 2.5.

The Ser-emb objects targeted by the ALMA and earlier CARMA observations (Enoch et al., 2011) were originally defined from large scale Bolocam 1.1 mm and Spitzer mid-IR surveys, and classified according to their bolometric temperature (Enoch et al., 2009). Most of the targets lie in two dense clusters: the northern Main Cluster (Ser-emb 4, 6, 8) and the southern Cluster B (Ser-emb 3, 7, 9, 11, 17). Three sources are relatively isolated (Ser-emb 2, 5, 15) from either cluster. An overview of the region showing these clusters and the locations of the targeted embedded sources can be found in figure 1 of Enoch et al. (2011).

Figures A.1-A.3 show the continuum maps with the full field of view for each of the ALMA pointings, and indicate the positions and IDs of c2d/GB YSOs by green pluses (Class 0+1, Flat Spectrum) and orange crosses (Class II). Red squares show the location of the postage-stamp views in figures 2.2 and 2.3.

Table A.1. Properties of the Serpens c2d+GB YSOs

Index	Spitzer Source Name (SSTc2d or SSTgb +)	A_V (mag)	Extinction Corrected α'	T_{bol}' (K)	L_{bol}' ($L_\odot$)	Class[a]	Associated ALMA Source ID	Field Ser-emb #
2776	J182854.0+002930	9.6	1.15	69	8.80	0+I	12	Ser-emb 7
2778	J182854.8+002952	9.6	1.60	51	6.60	0+I	5	Ser-emb 3,9
2779	J182854.9+001832	9.6	0.68	150	0.14	0+I	9	Ser-emb 5
2781	J182855.7+002944	9.6	1.65	26	1.60	0+I	15,16	Ser-emb 3,9
2803	J182906.2+003043	9.6	1.33	67	10.00	0+I	21	Ser-emb 11(W), 17
2804	J182906.7+003034	9.6	1.40	83	5.40	0+I	17,18	Ser-emb 11(W), 17
2811	J182909.0+003128	9.6	0.07	420	0.03	Flat	-	Ser-emb 1
2812	J182909.0+003132	9.6	2.13	36	4.20	0+I	1	Ser-emb 1
2865	J182948.1+011644	9.6	1.11	30	14.00	0+I	14	Ser-emb 8
2871	J182949.6+011521	9.6	2.53	13	69.00	0+I	11	Ser-emb 6
2882	J182952.3+003553	40.0	-1.55	2400	17.0	II	4	Ser-emb 2
2884	J182952.5+003611	9.6	0.54	68	1.90	0+I	2,3	Ser-emb 2
2887	J182953.0+003606	9.6	-0.35	890	0.58	II	-	Ser-emb 2, 15
2895	J182954.3+003601	9.6	-0.33	59	1.70	II	20	Ser-emb 15
2927	J182959.9+011311	9.6	2.20	120	7.00	0+I	6	Ser-emb 4 (N)
2932	J183000.7+011301	9.6	1.52	29	8.10	0+I	7	Ser-emb 4 (N)

Note. — This table adapted from table 2 of Dunham et al. (2015).

[a]Classes are defined by the extinction corrected spectral index α' as Class 0+I: $\alpha' \geq 0.3$, Flat-spectrum: $-0.3 \leq \alpha' < 0.3$; Class II: $-1.6 \leq \alpha' < -0.3$; and Class III: $\alpha' < -1.6$ (Greene et al., 1994).

A.1 Ser-emb 1

Ser-emb 1 is seen in the ALMA maps as a bright (100 mJy beam^{-1}) point-like source (ID 1) surrounded by faint, marginally detected (3σ) emission extending to the North-East. This extended structure is likely a component of the bright emission visible on $\sim 10''$ scales in the short-spacing CARMA maps of Enoch et al. (2011), which the ALMA observations are mostly insensitive to.

Ser-emb 1 is the Class 0 source with the lowest bolometric temperature (39K) in Serpens Main (Enoch et al., 2009), suggesting it is also the least evolved. A N-S oriented bi-polar jet likely originating from Ser-emb 1 is seen in 2.122 μm H_2 emission (Djupvik et al., 2016). N-S oriented CO outflows are also seen emanating directly from the source in CO (J = 2 $\rightarrow$ 1) Hull et al. (2014).

Two c2d/GB YSOs (Dunham et al., 2015) are found within a few arcseconds of source 1. The closer YSO, 2812, has a lower T_{bol}(36 K), similar to that found by Enoch et al. (2009). YSO 2811 is a warmer (420 K) source with no corresponding mm emission visible in the ALMA maps, which is perhaps unsurprising given its very low bolometric luminosity (0.03 $L_\odot$) and more evolved flat spectrum classification.

Ser-emb 1 is coincident (to within $\sim 2''$) with a 3.6 cm radio continuum source detected by the VLA, which may result from thermal free-free emission in shocks (Djupvik et al., 2006).

A.2 Ser-emb 2

Three compact, faint ($<$ 10mJy beam^{-1}) sources (IDs 2-4) are found in the maps of ALMA Ser-emb 2. Enoch et al. (2011) detected these sources only at a 5σ level in preliminary 110 GHz maps, but did not follow up with 230 GHz (1.3 mm) observations as was done for the other Ser-emb objects due to their faintness.

The central sources in the map correspond to the location of Ser-emb 2 and consist of a disk-like ($\sim$ 275 AU major axis) component (ID 2) connected to a point source (ID 3) by a small ridge of emission. The c2d/GB YSO 2884 is coincident with source 2 and has $T_{bol} = 68$ K.

The source at the southern edge of the field (ID 4) also appears to be a compact resolved disk ($\sim$ 257 AU major axis), and is associated with c2d/GB YSO 2882. This class II YSO is more evolved and the hottest in the sample, with a $T_{bol} = 2400$ K. It is also the most optically extincted at $A_V = 40$, compared to the $A_V = 9.6$ for all other YSOs in these fields.

Gould Belt YSO 2887 appears within the field, but with no corresponding mm emission, possibly because of its more evolved Class II status and lower luminosity ($L_{bol} = 0.58 L_{\odot}$). This YSO is also seen on the edge of the adjacent Ser-emb 15 field.

A.3 Ser-emb 3 and 9

Ser-emb 3 and 9 are located close enough together ($\sim 15''$ apart) that they are both seen in two of the ALMA pointings. Neither were mapped at 230 GHz by Enoch et al. (2011) due to the lack of clear detections in 110 GHz maps.

Ser-emb 3 is seen as a faint ~ 9 mJy beam^{-1} point source (ID 5) associated with the c2d/GB YSO 2778, a $T_{bol} = 51$ K class 0+I object.

Ser-emb 9 appears as a tight pair of ~ 9 mJy beam^{-1} peaks (IDs 15, 16) separated by just $\sim 0.5''/215$ AU and embedded in fainter emission. It is associated with the Gould Belt YSO 2781, a Class 0+1 source with $T_{bol} = 26$ K. Ser-emb 9 is also seen associated with a 3.6 cm radio to within $1''$ (Djupvik et al., 2006).

A.4 Ser-emb 4 (N)

ALMA observations of this field detect three faint (< 3 mJy/beam) point sources (IDs 6, 7, 8). In the CARMA observations, three regions of extended emission are detected and named Ser-emb 4 S, E, and N. Ser-emb 4 N is the brightest component of this CARMA source, but due to its extended nature, the ALMA configuration barely detects it at the field center. The ALMA observations find the Eastern-most point source (Source 8) is coincident with Ser-emb 4 E, but do not detect the fainter envelope around the source seen by CARMA. Ser-emb 4 S is similarly undetected.

The point source East of Ser-emb 4 N (Source 7) is associated with c2d/GB YSO 2932, a class 0+I source with $T_{bol} = 28$ K. Since no compact mm emission or mid-IR c2d/GB sources are found at the positions of Ser-emb N and S, these sources are likely pre-stellar in nature.

The Northern-most point source (Source 6) in this field is identified as Ser-emb 19, a class I with $T_{bol} = 129$ K in Enoch et al. (2009). It is also associated with Gould Belt 2927, a Class 0+I found to have a similar $T_{bol} = 120$ K.

A.5 Ser-emb 5

A single 7.8 mJy beam^{-1} point source (ID 9) is found at the field center of the ALMA observations. Enoch et al. (2011) similarly detect a faint point source, and suggest the object is the precursor to a brown dwarf or in a very low state of accretion due to its low luminosity ($L_{bol} = 0.4 L_{\odot}$). The Class 0+I c2d/GB YSO 2779 is found at the position of this source, and has $T_{bol} = 129$ K and a low luminosity ($L_{bol} = 0.14 L_{\odot}$.

A.6 Ser-emb 6

Ser-emb 6 [also known as Serpens FIRS 1 (Harvey et al., 1984) and SMM 1 (Casali et al., 1993)] is the brightest Class 0 source in Serpens Main and one of the most extensively studied. CARMA observations of the source found an extended envelope surrounding two resolved sources. In the ALMA observations, two extremely bright resolved sources are seen ($\sim$ 1000 mJy beam^{-1}, ID 10 and $\sim$ 100 mJy beam^{-1}, ID 11) surrounded by complex extended structure. For consistency with other high-resolution ALMA observations of this object [e.g Hull et al. (2016)], the bright central source will be referred to as SMM1-a and the relatively fainter western source will be called SMM1-b.

SMM1-a and b are associated with several jets and outflows. Hull et al. (2016) find high velocity $\sim$ 80 km/s CO ($J = 2 \rightarrow 1$) jets emanating from SMM1-a and b. They interpret the C-shaped extended structure around SMM1-a as walls of a cavity carved by precession of the jet. The same cavity is also seen in free-free emission from VLA observations, which Hull et al. (2016) suggest to be caused by ionization of gas in shocks at the cavity walls. Polarization measurements with ALMA suggest that the jets are playing a role in shaping the local magnetic field (Hull et al., 2017a). Lower velocity ($\sim 10 - 20$ km/s) wide angle outflows are also seen in the CO ($J = 2 \rightarrow 1$) emission around the high velocity jets Hull et al. (2014, 2017a). Mid-IR Spitzer observations also find jets in H_2 and various atomic emission lines (e.g. [FeII]), however, interpreting which source is driving each outflow is complicated by the complexity of the outflows and lower Spitzer resolution (Dionatos et al., 2014).

One c2d/GB YSO, 2871, is found coincident with SMM1-b, however, given that the beam size of Spitzer ranges 2.5″to 40″depending on the instrument and wavelength, flux from the brighter SMM1-a is almost certainly a large contribution if not dominating contribution to the YSO's determined properties. Its low temperature ($T_{bol} = 13$ K) and high luminosity ($L_{bol} = 69 L_{\odot}$) agree well with the classification of

Ser-emb 6 as a bright Class 0 source by Enoch et al. (2009). The coincidence of 2871 with source SMM1-a rather than b could also indicate that a is fainter at mid-IR wavelengths, but higher resolution observations would be needed to confirm this.

SMM1 is the only source in the Serpens sample which is confirmed to be variable at sub-mm wavelengths. It has been rising in brightness by $\sim 5\%\mathrm{yr}^{-1}$ in the first 18 months of the JCMT Transient Survey from December 2017 to June 2018 (Johnstone et al., 2018) and by $\sim 2\%\mathrm{yr}^{-1}$ from 2012 to 2016 in comparisons of archival Gould Belt Survey and Transient survey data (Mairs et al., 2017b). Future epochs of ALMA observations should be able to determine if SMM1-a or b is the source of the rising brightness provided this trend continues.

A.7 Ser-emb 7

Ser-emb 7 is detected in the ALMA observations as a ~ 17 mJy beam^{-1} point source (ID 12) surrounded by complex and filamentary extended structure of ~ 1000 AU in size. This is suggestive of a fragmenting disk or interaction with outflows. No outflows in Spitzer maps of the Cluster B region are linked to the structure surrounding Ser-emb 7, however, the source has yet to be observed at high resolution in CO or another tracer. Ser-emb 7 and extended structure are also seen in the CARMA observations, where maps constructed from large scale visibilities show an envelope extending $\sim 15''$ to the South of the source which is resolved out by the ALMA configuration.

The Class 0+I c2d/GB YSO 2776 is associated with Ser-emb 7. It is found to have a ($T_{bol} = 60$K), similar to the ($T_{bol} = 58$K) for Ser-emb 7 in Enoch et al. (2009). Ser-emb 7 is also associated with a 3.6 cm radio continuum source Djupvik et al. (2006) $5''$ to the North.

A.8 Ser-emb 8/S68N

Ser-emb 8 [Also known as S68N (McMullin et al., 1994) and SMM 9 Casali et al. (1993)] is detected in the ALMA maps as a ~ 30 mJy beam^{-1} point source (ID 14) surrounded by knotty extended emission. Another point source (ID 13) surrounded by extended structure is also detected to the North-East in the observations, here-after referred to as Ser-emb 8N. In the CARMA observations, large scale emission joins together the Ser-emb 8N and 8 in large scale maps. Both 8 and 8N power molecular outflows observed in SiO ($J = 5 \rightarrow 4$) extending SE-NE (Hull et al., 2014). Maps of this source in polarized dust emission find that magnetic fields at the 100-1000 AU

scales are weak and randomly oriented, suggesting turbulence plays a dominant role in establishing the field morphology at these scales Hull et al. (2017b).

Greene et al. (2018) have recently analysed a near-IR spectrum of Ser-emb 8 and detected features of the stellar photosphere (the first such detection and analysis for a Class 0 protostar), finding a photosphere temperature similar to pre-main-sequence stars, but with a lower surface gravity and larger stellar radius.

One class 0+1 Gould Belt YSO, 2865 is associated with Ser-emb 8, lying about 2″to the North of the bright central peak. No c2d/GB YSOs are associated with Ser-emb 8N, suggesting that it is too faint and/or deeply embedded to be detected at mid-IR wavelengths.

A.9 Ser-emb 11 (W) and 17

Ser-emb 11 and 17 are located $\sim 10''$ apart, and are thus seen in two of the ALMA pointings. 5 sources are found in both pointings (IDs 17-22). In both the ALMA and CARMA observations, Ser-emb 11 and 17 are detected and Ser-emb 11 is resolved into two components (IDs 17, 18). Both the targeted objects are bright, with peak fluxes of ~ 31 and ~ 42 mJy beam^{-1} for Ser-emb 11 (W) (ID 17)and 17 (ID 21) respectively. Some extended emission is seen around Ser-emb 11 and 17 in the ALMA maps.

Two previously unrecognized point sources (IDs 19, 22) are also found in the field. Both are faint, with a peak flux of ~ 3 (ID 19) and ~ 7 (ID 22) mJy beam^{-1}. Comparing the positions of these faint sources with the large scale CARMA maps in figure 3 of Enoch et al. (2011), there is some extended emission around the brighter ~ 7 mJy beam^{-1} source directly West of Ser-emb 11 (W), but none around the faint source North-East of Ser-emb 11 (W). The faintness of these sources makes them qualitatively similar to Ser-emb 5, and thus they might also be proto-Brown dwarfs or objects in very low level accretion states. However, no Gould Belt YSOs are associated with either object, nor can the possibility of a background sub-mm galaxy be ruled out, making such an interpretation insecure.

Ser-emb 11 and 17 have both been suggested as candidate driving sources for outflows seen in 2.122 μm H_2 by Spitzer Djupvik et al. (2016). Outflows are also seen closer to each source in CO ($J = 2 \rightarrow 1$) Hull et al. (2014).

Ser-emb 11 E (ID 18) is associated with c2d/GB YSO 2804, a $T_{bol} = 67$K source, and Ser-emb 17 is similarly associated with YSO 2803, a $T_{bol} = 73$K source. Similar

bolometric temperatures are found by Enoch et al. (2009), who place both objects in Class I. Ser-emb 11 is additionally associated with a 3.6 cm continuum source less than $\sim 1''$ away Djupvik et al. (2006).

A.10 Ser-emb 15

Ser-emb 15 is detected in both the ALMA and CARMA observations, and a disk-like ($\sim$ 126 AU major axis) source (ID 20) with a $\sim$ 35 mJy beam^{-1} peak is seen in the ALMA observations.

Ser-emb 15 is associated with c2d/GB YSO 2895, a marginal class II ($\alpha' = -0.33$) source with $T_{bol} = 120$K, the warmest of the targeted Ser-emb objects. Enoch et al. (2009) place Ser-emb 15 in Class I with $T_{bol} = 100$K, which is likely a more appropriate categorization of the object given the extended disk seen in these ALMA observations.

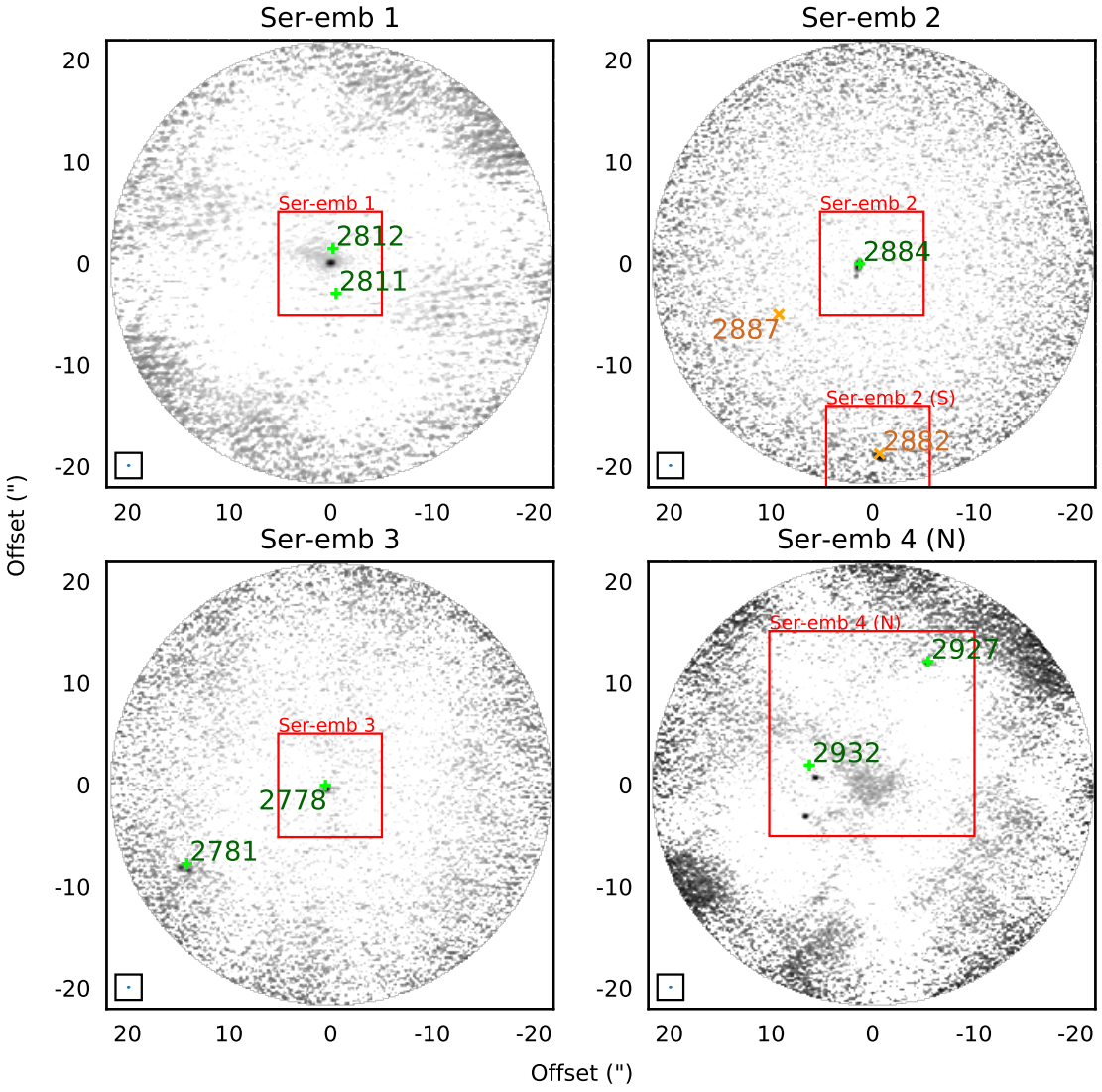

Figure A.1 Full maps of the ALMA observations of deeply embedded Serpens protostars. Red squares indicate the field of view for the postage stamps in figures 2.2 and 2.3. The maps are shown with primary beam correction to indicate ALMA's field of view.

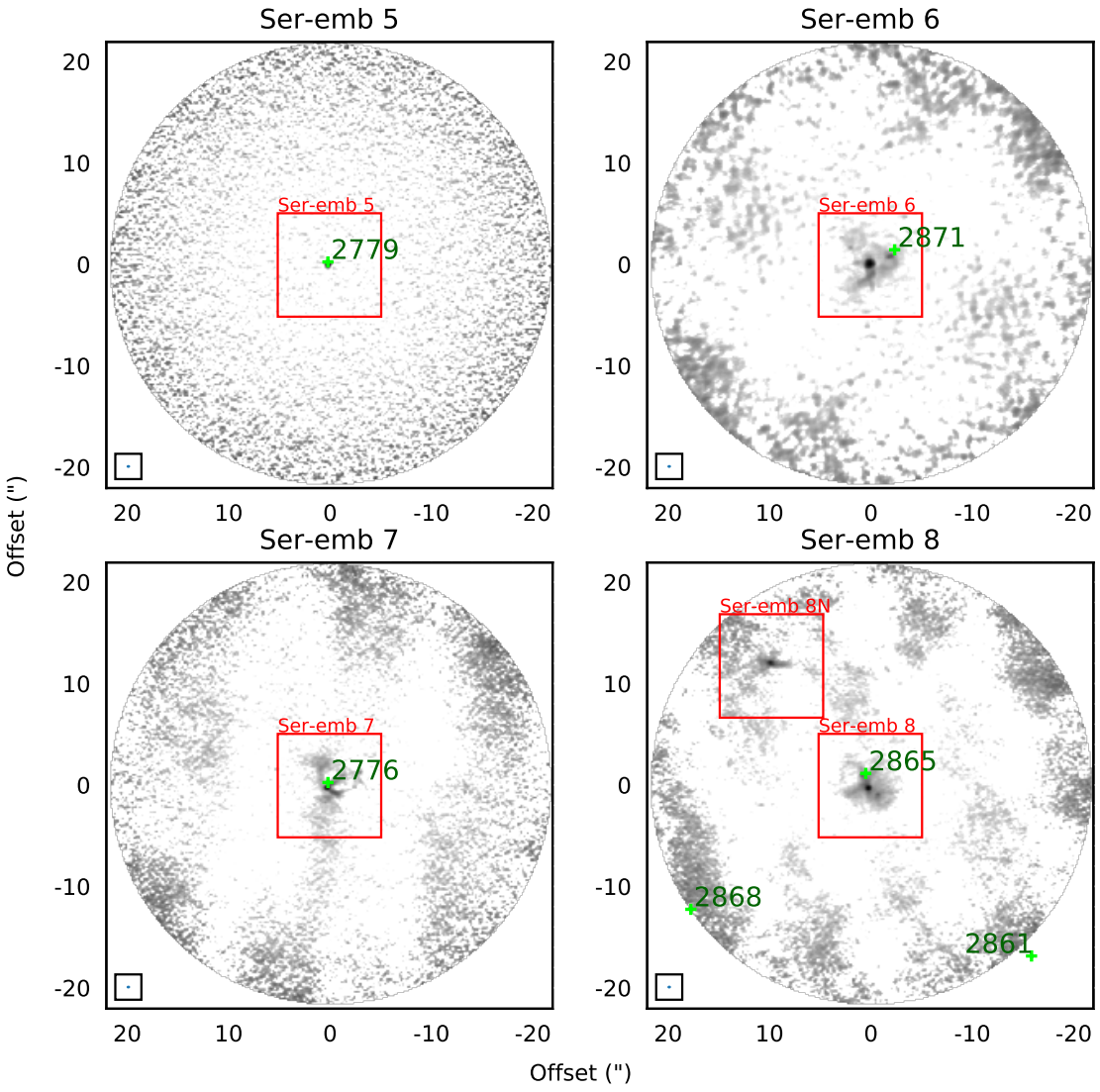

Figure A.2 As figure A.1.

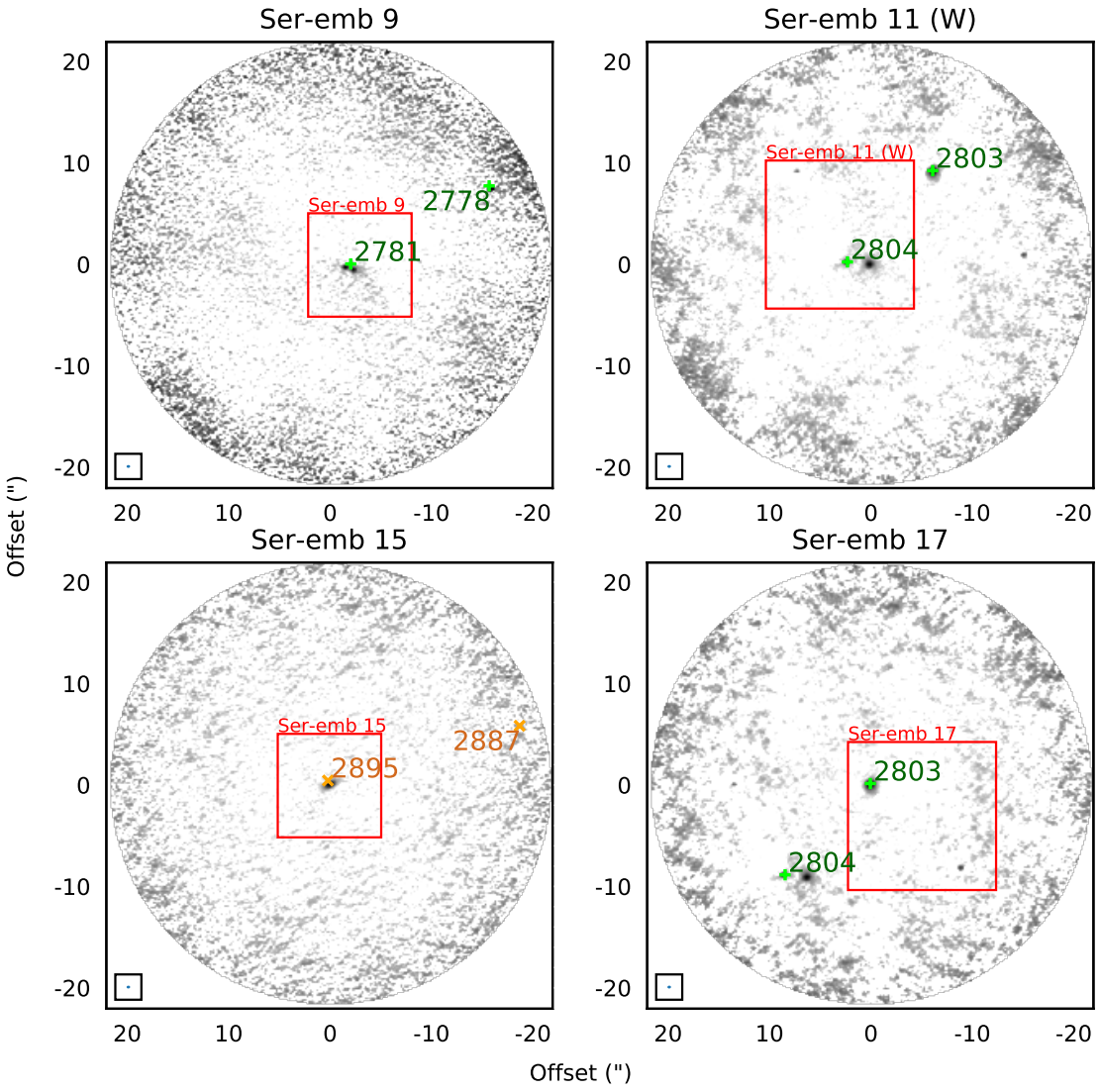

Figure A.3 As figure A.1.

Bibliography

Armitage, P. J., Livio, M., & Pringle, J. E. 2001, MNRAS, 324, 705

Audard, M., Ábrahám, P., Dunham, M. M., et al. 2014, Protostars and Planets VI, 387

Bae, J., Hartmann, L., Zhu, Z., & Nelson, R. P. 2014, ApJ, 795, 61

Bergin, E. A., & Tafalla, M. 2007, ARA&A, 45, 339

Bonnell, I., & Bastien, P. 1992, ApJ, 401, L31

Briggs, D. S. 1995, PhD thesis, The New Mexico Institute of Mining and Technology

Casali, M. M., Eiroa, C., & Duncan, W. D. 1993, A&A, 275, 195

Cha, S.-H., & Nayakshin, S. 2011, MNRAS, 415, 3319

Chen, H., Myers, P. C., Ladd, E. F., & Wood, D. O. S. 1995, ApJ, 445, 377

Clark, B. G. 1980, A&A, 89, 377

Conway, J. E., Cornwell, T. J., & Wilkinson, P. N. 1990, MNRAS, 246, 490

Cornwell, T. J. 2008, IEEE Journal of Selected Topics in Signal Processing, 2, 793

Costigan, G., Vink, J. S., Scholz, A., Ray, T., & Testi, L. 2014, MNRAS, 440, 3444

Dempsey, J. T., Friberg, P., Jenness, T., et al. 2013, MNRAS, 430, 2534

Dionatos, O., Jørgensen, J. K., Teixeira, P. S., Güdel, M., & Bergin, E. 2014, A&A, 563, A28

Djupvik, A. A., André, P., Bontemps, S., et al. 2006, A&A, 458, 789

Djupvik, A. A., Liimets, T., Zinnecker, H., et al. 2016, A&A, 587, A75

Dunham, M. M., Evans, II, N. J., Terebey, S., Dullemond, C. P., & Young, C. H. 2010, ApJ, 710, 470

Dunham, M. M., Stutz, A. M., Allen, L. E., et al. 2014, Protostars and Planets VI, 195

Dunham, M. M., Allen, L. E., Evans, II, N. J., et al. 2015, ApJS, 220, 11

Eiroa, C., Djupvik, A. A., & Casali, M. M. 2008, The Serpens Molecular Cloud, ed. B. Reipurth, 693

Enoch, M. L., Evans, II, N. J., Sargent, A. I., & Glenn, J. 2009, ApJ, 692, 973

Enoch, M. L., Glenn, J., Evans, II, N. J., et al. 2007, ApJ, 666, 982

Enoch, M. L., Corder, S., Duchêne, G., et al. 2011, ApJS, 195, 21

Greene, T. P. 2001, American Scientist, 89, 316

Greene, T. P., Gully-Santiago, M. A., & Barsony, M. 2018, ApJ, 862, 85

Greene, T. P., Wilking, B. A., Andre, P., Young, E. T., & Lada, C. J. 1994, ApJ, 434, 614

Hartmann, L., Herczeg, G., & Calvet, N. 2016, ARA&A, 54, 135

Hartmann, L., & Kenyon, S. J. 1996, ARA&A, 34, 207

Harvey, P. M., Wilking, B. A., & Joy, M. 1984, ApJ, 278, 156

Harvey, P. M., Rebull, L. M., Brooke, T., et al. 2007, ApJ, 663, 1139

Herbig, G. H. 1977, ApJ, 217, 693

—. 2008, AJ, 135, 637

Herczeg, G. J., Johnstone, D., Mairs, S., et al. 2017, ApJ, 849, 43

Heyer, M., & Dame, T. M. 2015, ARA&A, 53, 583

Hodapp, K. W. 1999, AJ, 118, 1338

Hodapp, K. W., Chini, R., Watermann, R., & Lemke, R. 2012, ApJ, 744, 56

Högbom, J. A. 1974, A&AS, 15, 417

Holland, W. S., Bintley, D., Chapin, E. L., et al. 2013, MNRAS, 430, 2513

Hull, C. L. H., Plambeck, R. L., Kwon, W., et al. 2014, ApJS, 213, 13

Hull, C. L. H., Girart, J. M., Kristensen, L. E., et al. 2016, ApJ, 823, L27

Hull, C. L. H., Girart, J. M., Tychoniec, Ł., et al. 2017a, ApJ, 847, 92

Hull, C. L. H., Mocz, P., Burkhart, B., et al. 2017b, ApJ, 842, L9

Hunter, T. R., Brogan, C. L., Megeath, S. T., et al. 2006, ApJ, 649, 888

Hunter, T. R., Brogan, C. L., MacLeod, G., et al. 2017, ApJ, 837, L29

Jensen, S. S., & Haugbølle, T. 2018, MNRAS, 474, 1176

Johnstone, D., Hendricks, B., Herczeg, G. J., & Bruderer, S. 2013, ApJ, 765, 133

Johnstone, D., Herczeg, G. J., Mairs, S., et al. 2018, ApJ, 854, 31

Kenyon, S. J., Hartmann, L. W., Strom, K. M., & Strom, S. E. 1990, AJ, 99, 869

Larson, R. B. 1981, MNRAS, 194, 809

Liu, H. B., Dunham, M. M., Pascucci, I., et al. 2017, ArXiv e-prints, arXiv:1710.08686

Lodato, G., & Clarke, C. J. 2004, MNRAS, 353, 841

Machida, M. N., Inutsuka, S.-i., & Matsumoto, T. 2011, ApJ, 729, 42

Mairs, S., Lane, J., Johnstone, D., et al. 2017a, ApJ, 843, 55

Mairs, S., Johnstone, D., Kirk, H., et al. 2017b, ApJ, 849, 107

McKee, C. F., & Offner, S. R. R. 2011, in IAU Symposium, Vol. 270, Computational Star Formation, ed. J. Alves, B. G. Elmegreen, J. M. Girart, & V. Trimble, 73–80

McMullin, J. P., Mundy, L. G., Wilking, B. A., Hezel, T., & Blake, G. A. 1994, ApJ, 424, 222

McMullin, J. P., Waters, B., Schiebel, D., Young, W., & Golap, K. 2007, in Astronomical Society of the Pacific Conference Series, Vol. 376, Astronomical Data Analysis Software and Systems XVI, ed. R. A. Shaw, F. Hill, & D. J. Bell, 127

Myers, P. C., & Ladd, E. F. 1993, ApJ, 413, L47

Nayakshin, S., & Lodato, G. 2012, MNRAS, 426, 70

Ortiz-León, G. N., Dzib, S. A., Kounkel, M. A., et al. 2017, ApJ, 834, 143

Pfalzner, S., Tackenberg, J., & Steinhausen, M. 2008, A&A, 487, L45

Plunkett, A. L., Arce, H. G., Mardones, D., et al. 2015, Nature, 527, 70

Rab, C., Elbakyan, V., Vorobyov, E., et al. 2017, A&A, 604, A15

Reipurth, B. 1990, in IAU Symposium, Vol. 137, Flare Stars in Star Clusters, Associations and the Solar Vicinity, ed. L. V. Mirzoian, B. R. Pettersen, & M. K. Tsvetkov, 229–251

Safron, E. J., Fischer, W. J., Megeath, S. T., et al. 2015, ApJ, 800, L5

Sault, R. J., Teuben, P. J., & Wright, M. C. H. 1995, in Astronomical Society of the Pacific Conference Series, Vol. 77, Astronomical Data Analysis Software and Systems IV, ed. R. A. Shaw, H. E. Payne, & J. J. E. Hayes, 433

Schwarz, U. J. 1978, A&A, 65, 345

Shu, F. H. 1977, ApJ, 214, 488

Shu, F. H., Adams, F. C., & Lizano, S. 1987, ARA&A, 25, 23

Simon, J. B., Hawley, J. F., & Beckwith, K. 2011, ApJ, 730, 94

Taquet, V., Wirström, E. S., & Charnley, S. B. 2016, ApJ, 821, 46

Tassis, K., & Mouschovias, T. C. 2005, ApJ, 618, 783

Venuti, L., Bouvier, J., Irwin, J., et al. 2015, A&A, 581, A66

Vorobyov, E. I., & Basu, S. 2005, ApJ, 633, L137

—. 2006, ApJ, 650, 956

—. 2010, ApJ, 719, 1896

Williams, J. P., Blitz, L., & McKee, C. F. 2000, Protostars and Planets IV, 97

Yoo, H., Lee, J.-E., Mairs, S., et al. 2017, ApJ, 849, 69

Zauderer, B. A., Bolatto, A. D., Vogel, S. N., et al. 2016, AJ, 151, 18

Zhu, Z., Hartmann, L., & Gammie, C. 2009a, ApJ, 694, 1045

—. 2010, ApJ, 713, 1143

Zhu, Z., Hartmann, L., Gammie, C., & McKinney, J. C. 2009b, ApJ, 701, 620